

THIS MANUSCRIPT HAS BEEN SUBMITTED FOR PUBLICATION IN GEOPHYSICAL JOURNAL INTERNATIONAL. PLEASE NOTE THAT DESPITE HAVING UNDERGONE PEER-REVIEW, THE MANUSCRIPT HAS NOT BEEN FORMALLY ACCEPTED YET FOR PUBLICATION AND, THEREFORE, IT MAY BE SUBJECT TO SOME CHANGES. SUBSEQUENT VERSIONS OF THE MANUSCRIPT MAY INCLUDE SLIGHTLY DIFFERENT CONTENT. IF ACCEPTED THE FINAL VERSION OF THE MANUSCRIPT WILL BE AVAILABLE THROUGH THE “PEER REVIEW PUBLICATION DOI” LINK.

1 **Paleomagnetism from multi-orogenic terranes is "not a**
2 **simple game": Pyrenees' Paleozoic warning**

3 Daniel Pastor-Galán^{1,2,3}, Oscar Groenhof⁴, Emilio L. Pueyo⁵, Esther
4 Izquierdo-Llavall⁶, Jaume Dinarès-Turell⁷, Mark J. Dekkers⁴

5 ¹Frontier Research Institute for Interdisciplinary Science, Tohoku University, Japan

6 ²Center for North East Asian Studies, Tohoku University, 980-8576, 41 Kawauchi, Aoba-ku, Sendai,
7 Miyagi, Japan

8 ³Department Earth Science, Tohoku University, Japan

9 ⁴Paleomagnetic Laboratory 'Fort Hoofddijk', Utrecht University, The Netherlands

10 ⁵Instituto Geológico y Minero de España (CN IGME-CSIC). Unidad de Zaragoza. Spain

11 ⁶Université de Pau et des Pays de l'Adour, E2S UPPA, CNRS, TOTAL, LFCR, Pau, France

12 ⁷Istituto Nazionale di Geofisica e Vulcanologia, Roma, Italy

13 **Summary**

14 Paleomagnetism is a versatile tool in the Earth sciences: it provides critical input to geological
15 time scales and plate tectonic reconstructions. Despite its undeniable perks, paleomagnetism is
16 not without complications. Remagnetizations overprinting the original magnetic signature of
17 rocks are frequent, especially in orogens which tend to be the areas with better rock exposure.

18 Unraveling the magnetic history of the rocks is a complicated task, especially in areas that
19 underwent several orogenic pulses. In turn, constraining the timing of remagnetization represents
20 an opportunity to solve post-magnetization structural and tectonic kinematics. Here, we evaluate
21 the magnetization history of Silurian-Devonian carbonates from the Axial Zone of the Pyrenees.
22 The Pyrenees are a multi-orogenic mountain belt where Silurian-Devonian rocks have seen the
23 Variscan collision (late Paleozoic), the opening of the Atlantic / Bay of Biscay (early
24 Cretaceous) and the Alpine orogeny (late Cretaceous to Miocene). Our results show widespread
25 remagnetization(s) carried by magnetite and pyrrhotite in the Silurian-Devonian series of the
26 Pyrenees. The majority of the samples show a post-folding but pre-alpine tilting magnetization.
27 Considering the equatorial inclinations found in such samples, we suggest that they likely
28 acquired their magnetization during the late Carboniferous and early Permian times. Two of the
29 studied sites (located at the western Axial Zone) were subsequently remagnetized at the end of
30 the Alpine orogeny. The paleomagnetic results constrained that the Variscan orogeny was
31 responsible for the main folding event affecting Paleozoic rocks in the Axial Zone, whereas the
32 Alpine orogeny produced the large-scale thrusting and antiformal stacking of these units. In
33 addition, we observed a general clockwise rotational pattern which could be related with the
34 formation of the Cantabrian Orocline and/or rotations associated with the Alpine orogeny. The
35 Silurian-Devonian carbonates are thus useful to understand the tectonic evolution of the
36 Pyrenean mountain range after a systematic combination of paleomagnetism with structural and
37 petrological observations. In contrast, the secondary character of magnetization and
38 complications associated with the Variscan tectonics indicate that a reassessment of Siluro-
39 Devonian poles from the Variscan elsewhere in Europe might be appropriate.

40 **Keywords**

41 Remagnetization, Pyrenees, Variscan, Alpine, Silurian-Devonian, oroclinal

42 1. Introduction

43 The Earth's magnetic field has left a remnant signature in the geological record through eons. These
44 magnetic signals in the rock archive have been crucial to almost any field of Earth Sciences, from the
45 development of plate tectonics (e.g., Vine and Matthews, 1963), to the development of global time
46 scales (e.g., Kuiper et al., 2008) or the origin and evolution of the core (e.g., Biggin et al., 2015).
47 Paleomagnetism is still the only available technique that can quantify pre-Jurassic paleolatitudes
48 (Domencier and Torsvik, 2019), intensities of the past magnetic field, or global reference times
49 through reversals. The paleomagnetic imprint in rocks can last billions of years but may be also
50 fragile. For example, remagnetizations that overprint or even delete the original magnetic signature
51 are ubiquitous, especially in orogenic belts (e.g., Pueyo et al. 2007, 2016a; Van der Voo and Torsvik,
52 2012; Huang et al. 2017). The majority of the studies associated with the preservation and
53 reacquisition of a magnetic remanence in rocks are relatively recent. Although remagnetizations were
54 initially recognized already during the 1960's and remarked its importance in the 1980's (McCabe et
55 al., 1983; McCabe and Elmore, 1989), they have been studied in particular detail only from the first
56 two decades of the 21st century onward (c.f. van der Voo and Torsvik, 2012). Since then
57 paleomagnetists and rockmagnetists have realized to the full that a plethora of chemical and physical
58 processes are capable of resetting the magnetic signature in a rock (e.g., Jackson et al., 1993; Weil
59 and van der Voo., 2002; Dekkers, 2012; Pastor-Galán et al., 2017; Aubourg et al., 2019; Huang et al.,
60 2020).

61 Remagnetization is often deemed a problem because it interferes with paleogeographic
62 reconstructions that rely on the analysis of primary natural remanent magnetization (NRM), i.e. the

63 age of the NRM is the same as the age of the sampled rock unit. Despite the perceived loss of
64 information, remagnetized rocks do represent valuable sources of geological information when it is
65 possible to retrieve precisely the timing of the resetting of the original NRM acquisition, i.e. the
66 remagnetization. Remagnetized rocks have been successfully used to unravel paleolatitudes of
67 orogenic processes, orogenic kinematics, as geothermometers, to reconstruct inverted basins, ...
68 (e.g., Dinarès-Turell and García-Senz, 2000, Huang et al., 2015; Villalaín et al., 2016; Aubourg et al.,
69 2019; Izquierdo-Llavall et al., 2020). Rocks with complex orogenic histories – the rule in many
70 orogens – present a myriad of complications including the timing of their NRM acquisition. In such
71 settings, paleomagnetism can be an excellent tool to understand multiphase orogenic systems (and
72 remagnetizations helpful to observe snapshots of deformation histories) if wisely used in concert
73 with other geologic tools.

74 Many paleomagnetic studies were performed before our current understanding of remagnetization
75 processes and for a given region, time frame, or lithology, those older paleomagnetic data may be
76 the only data available. There is an evident need to review and critically reassess such paleomagnetic
77 information: regional and even global geologic interpretations are still grounded in them. In this
78 paper, we reappraise the paleomagnetism from Silurian-Devonian limestones in the Pyrenean
79 mountain belt, from which only three rather limited studies have been previously published (Tait et
80 al., 2000; Gil-Peña et al., 2006; Izquierdo-Llavall et al., 2020). From these datasets, Tait et al. (2000)
81 interpreted that the magnetic signal carried by Silurian-Devonian units was primary and subsequent
82 plate reconstructions (e.g. Domeier and Torsvik, 2014) have relied on this suggested magnetization
83 age to create the Devonian paleogeography of Europe, but that date might have been remagnetized
84 or not corrected properly as witnessed by several younger studies (e.g. Izquierdo-Llavall et al., 2018
85 and references therein). Our results, together with an enhanced geologic and paleomagnetic
86 knowledge of the orogen, show that the sampled Silurian-Devonian carbonates were completely

87 remagnetized during the late Carboniferous and Early Permian, when they could experience
88 significant clockwise vertical axis rotations. These rocks were partially overprinted yet another time
89 during Cretaceous and Cenozoic times, and experienced extension, compression, tilting and vertical
90 axis rotations related to both the opening of the Bay of Biscay in the Late Mesozoic and the
91 Cenozoic building of the Alpine chain in the Pyrenees. The magnetization history of the Pyrenees is
92 a warning for paleomagnetists beautifully illustrated in Chris Scotese's anagram:
93 PALEOMAGNETISM = NOT A SIMPLE GAME (Van der Voo, 1993).

94 2. The Pyrenean mountain belt

95 The Pyrenees are a mountainous barrier that separates the Iberian Peninsula from the rest of
96 Eurasia. They are a prime example of the superposition of different tectonic events: (1) the
97 multiphase late Paleozoic Variscan orogeny; (2) the Jurassic and early Cretaceous major extension
98 resulting into the formation of oceanic crust in the Atlantic Ocean and the Bay of Biscay and the
99 exhumation of the mantle between the Neotethys and Atlantic Oceans along the current Pyrenees;
100 (3) the closure of this previously opened seaway in the late Cretaceous; and (4) the final collision
101 between the Iberian and Eurasian plates during the Cenozoic (Muñoz, 1992; 2019 and references
102 therein).

103 2.1 Paleozoic History: Variscan cycle

104 The tectonic evolution of the Paleozoic era was dominated by the progressive amalgamation of most
105 continents into Pangea (e.g., Domeier and Torsvik, 2014; Domeier, 2016), the latest supercontinent
106 (Pastor-Galán et al., 2019a). In western Europe the Pangean amalgamation history is recorded in the
107 Variscan orogen, which sutured the continents of Gondwana and Laurussia along with a variable
108 number of smaller plates that likely drifted away from Gondwana (e.g., Nance et al., 2010). On the

109 basis of paleomagnetic data, Iberia has been considered part of a ribbon continent (usually named
110 Armorica, Galatia, or Hun) that detached from Gondwana and drifted to the north or northwest in
111 the Late Silurian or Early Devonian (e.g., van der Voo, 1993; Tait et al., 2000; Tait, 1999; Stampfli et
112 al., 2013; Domeier and Torsvik, 2014). Other authors, however, place Iberia along the passive
113 margin of Gondwana throughout the Paleozoic based on the fossil record or the provenance of
114 detrital zircons (e.g., Robardet, 2003; Pastor-Galán et al., 2013a). Convergence leading up to the
115 Variscan orogen started ca. 420 Ma (e.g., Franke et al., 2017) and continued until the complete
116 consumption of the Rheic ocean and other minor oceanic basins that existed between Gondwana
117 and Laurussia at ca. 280 Ma; (e.g., Pastor-Galán, 2020). The final continent–continent collision was
118 diachronic and became progressively younger westwards (in present-day coordinates) with Devonian
119 continent–continent collision along the eastern boundary of the Variscan orogen, progressing to
120 earliest Permian ages in the westernmost sector (e.g., Pastor-Galán et al., 2020 and references
121 therein).

122 Iberia has the largest exposure of the Variscan orogen in Europe, and an almost continuous cross
123 section of the orogen (e.g., Azor et al., 2019). The majority of the Paleozoic outcrops in Iberia
124 contain Gondwanan affinity rocks (e.g., Pastor-Galán et al., 2013a; Casas et al., 2019) and only a little
125 sector of Southwest Iberia shows Laurussian affinity (e.g., Pérez-Cáceres et al., 2017).

126 Geographically, the external zones of the Gondwana margin are nested to the north into the core of
127 the Cantabrian Orocline (Fig. 1A), whereas the hinterland zones are to the west, center and
128 northeast of Iberia (Fig. 1A; e.g., Azor et al., 2019). The stratigraphy of the Gondwanan autochthon
129 consists of Neoproterozoic arc rocks (e.g., Fernández-Suárez et al., 2014), which evolved to a rift-to-
130 drift sequence during the Cambrian to early Ordovician and then to an Ordovician to late Devonian
131 passive margin basin sequence (e.g., Gutiérrez-Alonso et al., 2020). During the Carboniferous and

132 early Permian, the rocks recorded up to 6 phases of deformation (e.g., Dias da Silva et al., 2020;
133 Pastor-Galán et al., 2020 and references therein), metamorphism (e.g., Ribeiro et al., 2019) and
134 synorogenic sedimentation processes that evolved to post-orogenic and intracontinental style basins
135 during the Permian (e.g., Oliveira et al., 2019).

136 The trend of the Variscan belt in north Iberia follows a “C” shape known as the Cantabrian
137 Orocline (e.g., Pastor-Galán et al., 2020). The Cantabrian Orocline seems isoclinal, formed by a
138 northern and a southern E-W-trending limbs, but this is likely the product of a retightening during
139 the Alpine orogeny (e.g., Pastor-Galán et al., 2011; Leite Mendes et al., 2021; Fig. 1A). All kinematic
140 data studied so far support a model in which the Cantabrian Orocline formed due to secondary
141 vertical-axis rotation in a period of time later than 315 Ma and earlier than 290 Ma. Overall, the
142 southern limb of the orocline rotated counterclockwise (CCW) and the northern limb clockwise
143 (CW; e.g., Weil et al., 2013). Orocline formation postdates the main Variscan orogenic phases (e.g.,
144 Pastor-Galán et al., 2015a). The development of the Cantabrian Orocline implies the existence of a
145 roughly linear orogenic belt during the early Variscan closure of the Rheic Ocean (with an
146 approximately N–S orientation in present-day coordinates), which was subsequently bent in map-
147 view into an orocline during the late stages of Pangea's amalgamation. This interpretation is
148 grounded in extensive paleomagnetic, structural and geochronological studies (e.g., Weil et al., 2001;
149 Pastor-Galán et al., 2014; Shaw et al., 2015; Gutiérrez-Alonso et al., 2015; Pastor-Galán et al., 2018).

150 The Palaeozoic rocks of the Pyrenees form the backbone of the Pyrenean chain and crop out in two
151 areas (the Axial Zone and the Basque Massifs, to the east and west, respectively) that define an E-W
152 elongated strip unconformably overlain by Mesozoic and Cenozoic rocks (Fig. 1A and B). These
153 outcrops are geographically disconnected from neighboring Paleozoic outcrops of the Catalan
154 Coastal Range and Balearic zone to the southeast, the Mouthoumet and Montagne Noire (southern

155 French Central massifs) to the north, Corsica-Sardinia to the east and the Iberian Massif to the west
156 and southwest. The pre-Permian rocks of the Pyrenees recorded a polyphase deformation during the
157 Variscan orogeny with metamorphism that ranges from absent to high grade (e.g. Casas et al., 2019).
158 So far, no relics of early Variscan deformation and/or subduction related high pressure
159 metamorphism have been found. Most palaeogeographic reconstructions suggest that the Pyrenean
160 Paleozoic outcrops (Fig. 1) may be equivalent to the northern branch of the Cantabrian Orocline
161 (e.g. García-Sansegundo et al., 2011; Pastor-Galán et al., 2020). Deformation, structural style and
162 metamorphic grade show important differences along strike in the Pyrenees (Autran and García-
163 Sansegundo, 1996; Debon and Guitard, 1996) and a N-S zonation, with fold-related cleavage being
164 pervasive in the central and northern part of the Axial Zone but poorly developed in the south
165 (García-Sansegundo et al., 2011). The superposition of the later Mesozoic extension and subsequent
166 Alpine orogeny markedly complicate an integral interpretation of the Variscan portions of the
167 Pyrenees (see Casas et al., 2019). As a consequence, a comprehensive scheme integrating all the
168 available data is lacking despite decades of geological research (e.g., de Sitter and Zwart, 1959;
169 Kleinsmiede, 1960; Zwart, 1979; 1986). In general terms, the Silurian, Devonian and Carboniferous
170 successions show no to low-grade metamorphism and are composed of carbonates and shales (e.g.,
171 Casas et al., 2019). During the Carboniferous and Early Permian, the Pyrenees recorded an intense
172 igneous activity including syn- to post-kinematic plutonism and volcanism (Fig. 1B; e.g., Gleizes et
173 al., 1997, 2003; Denèle et al., 2011, 2014; Porquet et al., 2017), sometimes interpreted as subduction
174 related (e.g., Pereira et al., 2014).

175 2.2 Mesozoic to present day evolution: Alpine cycle

176 The final break-up of Pangea is marked with the opening of the Central and South Atlantic from late
177 Triassic times onward (e.g., Müller et al., 2019). During the Jurassic, Iberia was attached to Europe

178 and North America as another piece of Laurasia. In the Cretaceous, the breakup and spreading in
179 the North Atlantic led to the separation of the Iberian microplate from Eurasia, North America and
180 Africa (e.g., Vissers and Meijer, 2012). During the North Atlantic breakup, the Bay of Biscay
181 opened, leading to approximately 35° of counterclockwise (CCW) rotation of Iberia (Van der Voo,
182 1969; Neres et al., 2013; Nierrengarten et al., 2018) probably during the Aptian (Juárez et al., 1998;
183 Gong et al., 2008). The opening of the Bay of Biscay to the west got recorded in the Pyrenees with
184 the formation of a hyperextended margin with mantle exhumation during the Albian–Cenomanian
185 (e.g. Lagabrielle et al., 2010). The rotation of Iberia, together with the increased convergence
186 between Africa and Eurasia culminated in the collision between Iberia and Eurasia to form the
187 Pyrenean range during Late Cretaceous–Miocene in the frame of the Alpine orogeny (e.g., Muñoz,
188 2019).

189 Paleozoic rocks in the Pyrenees are involved in a doubly-verging, asymmetric fold-and-thrust system
190 with the main Alpine thrust sheets in the Axial Zone being South-verging (Muñoz 1992, 2019;
191 Barnolas et al., 2019). They provoked over 100 km of N-S shortening and the southward
192 displacement of the Palaeozoic rocks in the Axial Zone over the autochthonous basement in the
193 southern Pyrenean foreland. The outcrops of Paleozoic rocks in the Axial Zone have witnessed
194 more than 7000 meters of basement stacking (measured between the Balaitous peak where the top
195 basement crops out and the San Vicente drill core; Fig. 1B; Lanaja, 1987). The geometry and
196 kinematics of the thrust units affecting the Paleozoic rocks are not fully understood because of the
197 complex superposition of deformation events and the unclear relationships with cover units where
198 syntectonic sedimentation plays a key role to assign kinematic ages (Oliva-Urcia, 2018). Numerous
199 structural studies (e.g., Muñoz et al., 1986, 2019; Muñoz, 1992; Puigdefábregas et al., 1992; Teixell,
200 1996, Millán et al., 2000; Martínez-Peña and Casas, 2003; Casas et al., 2003; Millán et al., 2006;
201 Labaume et al., 2016; Labaume and Teixell, 2018) have identified a general Alpine piggy-back thrust

202 sequence affecting the Paleozoic rocks (Fig. 2). Besides, numerous fission-track data on granites
203 (Fitzgerald et al., 1999; Jolivet et al., 2007), on detrital rocks (Beamud et al., 2011; Bosch et al., 2016;
204 Labaume et al., 2016) as well as $^{40}\text{Ar}/^{39}\text{Ar}$ and U/Pb dating of samples directly taken from fault
205 planes (Abd Elmola et al., 2018) and calcite veins (Hoareau et al., 2021, see also recent reviews by
206 Oliva-Urcia, 2018 and Calvet et al., 2020, and references therein), have improved the knowledge on
207 the chronology of emplacement and exhumation of the basement units and their relationship with
208 the cover ones. Basement thrusts partly reactivated previous Variscan, late-Variscan and/or
209 Mesozoic structures. The Alpine structure defines an imbricate thrust system (Fig 2) with a
210 progressively increasing vertical overlap between the basement units from west (Fig. 2A; Teixell,
211 1996) to east where thrusts define an antiformal stack (Fig. 2C; Muñoz, 1992). Basement units in the
212 west include four thrusts in the central sector (Fig. 2b): Millares, Bielsa, Gavarnie and Guarga; and
213 an variable number in the western sector (Fig. 2a), including the Lakora-Eaux Chaudes, Gavarnie,
214 Guara-Gedré, Fiscal-Broto and Guarga thrusts. In the eastern sector (Fig. 2c) three main basement
215 units are recognized, from the North to the South: Nogueras-Gavarnie, Orri and Rialp. In the South
216 Pyrenean Zone, all these basement units connect with an imbricate fold-and-thrust system with
217 different Mesozoic and Cenozoic décollements (Upper/Middle Triassic evaporites, Cretaceous
218 shales, and Eocene marls and evaporites); their geometry is controlled by salt-tectonics and
219 Mesozoic inheritance (Millán et al., 2000; Huyghe et al., 2009; Labaume et al., 2016; Oliva-Urcia,
220 2018; Labaume and Teixell, 2018; Calvín et al., 2018; Santolaria et al., 2020; Muñoz et al., 2021).

221 Thrusting was associated with important foreland flexure and foreland succession deposition both in
222 the Northern Pyrenees (France; Biteau et al., 2006) and the Southern Pyrenees (Spain;
223 Puigdefàbregas, 1975). Foreland deposits partly covered the Paleozoic units of the Axial Zone in the
224 early orogenic stages and were subsequently exhumed and eroded (Beamud et al., 2011; Fillon and
225 Van der Beek, 2012). The early, maximum burial conditions in the sampled portion of the Axial

226 Zone are partly constrained by paleothermal studies in the overlying Meso-Cenozoic cover units
227 (Izquierdo-Llavall et al., 2013; Labaume et al., 2016). They indicate Cenozoic-age, maximum
228 temperatures of 160-190 °C in the Upper Cretaceous units of the western Axial Zone (Izquierdo-
229 Llavall et al., 2013) that increase up to ~250 °C in the Eocene turbidites to the center of the
230 Southern Pyrenean Zone. These values indicate that temperatures in the underlying Paleozoic rocks
231 could range between 200 and 250 °C during the Cenozoic. Locally, around the Panticosa intrusion,
232 peak burial temperatures may have reached about ~300 °C during the Oligocene (Bosch et al., 2016).
233 In the central Axial Zone, thermal models for the Paleozoic units of the Gavarnie and Orri units
234 reveal peak temperatures below 300°C that were attained during the Early Paleogene (Waldner,
235 2019). Cenozoic burial favored the development of Alpine cleavage in the western Axial Zone
236 (Choukroune and Séguret, 1972; Matte et al., 2000). Conversely, in the central Axial Zone Alpine
237 cleavage developed only locally, the main cleavage being Variscan in age (Muñoz, 1992).

238 2.3 Paleomagnetism in the Pyrenees

239 Paleomagnetic investigations in the Pyrenees commenced with the pioneering studies of Van der
240 Lingen (1960) and Schwarz (1963) in some Paleozoic rocks from the center of the Pyrenees. The
241 available database has grown substantially during the following decades due to the excellent outcrop
242 conditions (including world class stratigraphic sequences), the general exposure of synorogenic
243 material throughout the chain allowing an accurate dating of deformation, the existence of well-
244 exposed zones of lateral transference of deformation, etc. At present, the Pyrenean chain represents
245 one of the most densely and homogeneously sampled paleomagnetic databases worldwide (Pueyo et
246 al., 2017). Despite the quality and amount of paleomagnetic data in the Pyrenees, the Pyrenean
247 Paleozoic rocks have remained largely unexplored. In the Axial Zone, very few data are known from
248 sites older than Permian–Triassic red beds (Van Dongen, 1967; McClelland and McCaig, 1988, 1989;

249 Keller et al., 1994; Tait et al., 2000; Gil-Peña et al., 2006; Izquierdo-Llavall et al., 2014, 2020; Ramón
250 et al., 2016). And, to our knowledge, in the Pyrenees only three paleomagnetic studies collected and
251 analyzed a limited number of sites dating from older than late Carboniferous (Stephanian) age: Tait
252 et al. (2000), Gil-Peña et al. (2006), and Izquierdo-Llavall et al. (2020). The two latter studies found
253 the rocks remagnetized in the Late Carboniferous and Paleogene, respectively. Previous studies in
254 late Carboniferous and early Permian rocks (Izquierdo-Llavall et al., 2014) revealed shallow
255 inclinations and clockwise rotations of $\sim 40^\circ$. Gil-Peña et al. (2006) showed analogous rotations
256 ($\sim 50^\circ$ CW) for the Ordovician rocks, that probably were remagnetized during late Carboniferous
257 times.

258 The relatively good paleomagnetic control on undeformed areas in the vicinity of the Pyrenees (e.g.,
259 Garcés et al., 2020; Oliva-Urcia and Pueyo, 2019) allows to define a reliable reference paleomagnetic
260 direction and to understand the post-Variscan (late Permian to Eocene) magnetization and tectonic
261 history during the Alpine orogeny in the Pyrenees. In the South Pyrenean Zone, significant rotations
262 both CW and CCW ($40\text{-}60^\circ$) derived from proven primary paleomagnetic records from rocks of
263 ages ranging from Permo-Triassic (e.g., Larrasoña et al., 2003) to Oligocene (e.g., Sussman et al.,
264 2004) are found in the most external cover units in relation to lateral ramps in thrust sheets. These
265 rotations are especially evident nearby the boundaries of the so-called South Pyrenan Central Unit
266 (e.g., Sussman et al., 2004; Mochales et al., 2012, 2016; Muñoz et al., 2013; Rodríguez-Pintó et al.,
267 2016) but also in the most external thrust units (Pueyo et al., 2021a, 2021b). Other moderate vertical
268 axis rotations ($15\text{-}25^\circ$ CW and CCW, locally attaining $\sim 40^\circ$) occur in the Permo-Mesozoic structural
269 units immediately to the south of the Axial Zone: The Internal Sierras (Larra-Monte Perdido units;
270 Oliva-Urcia and Pueyo, 2007a, 2007b; Oliva-Urcia et al., 2008; Izquierdo-Llavall et al., 2015), the
271 Nogueras thrust and underlying units (McClelland and McCaig, 1988, 1989; Dinarès et al., 1992;
272 Oliva-Urcia et al., 2012; Izquierdo-Llavall et al., 2018) and in the eastern Cadi unit (Dinarès et al.,

273 1992; Keller et al., 1994; Pueyo et al., 2016b). In the North Pyrenean Zone (France, Fig. 1B),
274 paleomagnetic data are scarcer and evidence strong (over 70° CW in Aptian-Albian rocks, Oliva-
275 Urcia et al., 2010; Rouvier et al., 2012) to null (Izquierdo-Llavall et al., 2020) vertical axis rotations in
276 different areas.

277 Early Cretaceous remagnetizations are relatively common in the Cretaceous basins deformed to the
278 south of the Axial Zone (e.g. Larrasoña et al., 2003; Garcés et al., 2016). However, this event have
279 been described, so far, only out of the Axial Zone. These remagnetizations are local and affect
280 compartmentalized and highly subsident basins developed under high thermal gradient conditions
281 (e.g., Lagabrielle et al., 2010) which played a key role to chemically remagnetize these rocks (e.g.,
282 Dinarès-Turell and García-Senz, 2000; Gong et al., 2008; 2009). On top of that, Cenozoic
283 remagnetizations have been described in the Meso-Cenozoic units just above the Axial Zone (Oliva
284 et al., 2008; 2012; Izquierdo-llavall et al., 2015). These Cenozoic remagnetizations likely occurred due
285 to the burial associated with the development of the Pyrenean orogenic wedge and southern
286 foreland basin. The wedge generated important lithostatic and tectonic load in the internal units until
287 the final collision, continentalization and exhumation of the Paleozoic rocks during Oligocene-
288 Miocene times.

289 Most of the paleomagnetic data to the south of the Axial Zone recorded, at least partially, Eocene
290 secondary magnetizations (pre, syn and postfolding). Remanent magnetization in the Mesozoic units
291 immediately to the North of the Axial Zone is in general terms post-folding and has been
292 interpreted as a Cenozoic chemical (Oliva-Urcia et al., 2010) or thermal (Izquierdo-Llavall et al.,
293 2020) remagnetization.

294 3. Sampling, methods and results

295 We drilled in 19 limestone sites from the Silurian or Devonian, one site of a late Carboniferous-early
296 Permian granite (OG01, Panticosa intrusion) and one Permian dyke that intruded the surroundings
297 of site OG12 (OG12dyke; Fig. 1B; Table 1) with a petrol-powered drill, in total 240 cores. We also
298 collected 6 oriented hand samples (from the OG07 and OG08 sites, three samples each). Sites are
299 distributed along-strike the southern and central Axial Zone from the Gallego valley in the west to
300 the Valira valley in the east in eight different valleys (Fig. 1B; the kml file `sample_locations.kml` with
301 exact locations is in the Supplementary material). Sites BN1 and OR15 were collected in the same
302 area of sites published in Tait et al. (2000). Several sites allowed field tests: five site-scale fold-tests
303 could be obtained (OG2; OG11; OG13; OG14; OG19); two tilt tests between sites within the same
304 thrust unit (OG3-4; BN1-OR15), and two sites with a baked contact test (OG12 and OG17). We
305 performed all analyses at Paleomagnetic Laboratory Fort Hoofddijk, Universiteit Utrecht, The
306 Netherlands.

307 Our sample collection comes from fresh, non metamorphic and weakly or non-internally deformed
308 sites. Limestones were sedimented in shallow waters usually associated with clastic and pelitic
309 sediments (Casas et al., 2019). Most limestone sites contained variable amounts of organic matter
310 visible while drilling. A few of these sites show a spaced solution cleavage and evidence of
311 recrystallization. We collected the bedding orientation and, when observable, that of the pressure-
312 solution cleavage (Table 1).

313 3.1 Alpine tilt estimation

314 The sampled rocks were affected by both Variscan and Pyrenean orogenies (Alpine). In the Axial
315 Zone, the Pyrenean orogeny produced the development of a south vergent fold-and-thrust system.

316 Its geometry has been extensively investigated in previous studies that reconstruct the Axial Zone
317 structure using a combination of surface data and seismic profiles (Labaume et al., 1985; Cámara and
318 Klimowitz, 1985; Muñoz, 1992; Teixell, 1996; Teixell and Muñoz, 2000; Martínez-Peña and Casas-
319 Sainz, 2003; Izquierdo-Llavall et al., 2013; Labaume et al., 2016; Muñoz et al., 2018; Labaume and
320 Teixell, 2018). These studies reveal that the Axial Zone evolves laterally from an imbricate thrust
321 system in the West (Fig. 2a, Teixell, 1996) to an antiformal-stack in the East (Fig. 2c, Muñoz, 1992).
322 Alpine thrusts are related to kilometric-scale basement folds in their hangingwalls. Basement folding
323 is well recorded by the Mesozoic units unconformably overlying the Paleozoic rocks and resulted in
324 dominantly southward and northward tilts in the southern and northern part of the Axial Zone,
325 respectively.

326 We used the available geological maps (GEODE, Robador et al., 2019) , including numerous
327 bedding data, and published cross-sections to discriminate the effects of Variscan and Pyrenean
328 orogenies and estimate the alpine tilt related to basement thrusting in our sampling sites. In the sites
329 located in the southern part of the Axial Zone, alpine dip directions and dips (Table 1) were
330 estimated from the average orientation of bedding in the Mesozoic units unconformably overlying
331 the Paleozoic and tested against the dip estimated in cross-sections. Sites in the central part of the
332 Axial Zone (OG11 to OG19) are too far away from Mesozoic cover units. In these sites, we defined
333 dip directions as perpendicular to alpine thrusts in the Paleozoic rocks. Following the dip direction
334 we projected our sampling points into the traces of previously published cross-sections to obtain the
335 dip (Fig. 2). Alpine dips were also estimated considering the Mesozoic geometries reconstructed
336 above the topography in such cross-sections (Fig. 2). Figure 2 provides a general picture of the
337 structural position of the sampled sites (see corresponding thrust units in Table 1) and the regional
338 alpine tilt recorded by the Mesozoic cover of the Axial Zone. Cross-sections run perpendicular to
339 the main alpine structures and therefore show true alpine dips. Apart from the regional cross-

340 sections shown in Figure 2 (Teixell, 1996; Muñoz, 1992; Martínez-Peña and Casas-Sainz, 2003), we
341 also took into account additional cross-sections located closer to the sampling sites (Izquierdo-
342 Llavall et al., 2013, 2018; Labaume and Teixell, 2018).

343 3.2 Paleomagnetic and Rock magnetic Methods

344 Knowing when and how rocks magnetized is crucial to obtain an appropriate interpretation of
345 paleomagnetic results, especially in terms of plate and structural kinematics. In this paper we
346 combined rock magnetic, paleomagnetic and structural geology analyses to unravel the
347 magnetization history of the rocks.

348 Rock magnetism studies the magnetic properties of rocks and their magnetic minerals. The different
349 magnetic properties of rocks, such as magnetic hysteresis, susceptibility and its anisotropy,
350 magnetization vs. temperature (thermomagnetic analysis), can inform about the mineral(s) carrying
351 the magnetic remanence and their crystal structure and grain size. This information is the most
352 important to understand the geological processes involved in the magnetization of the rocks, and
353 eventually also a key to unravel magnetization timings. In this research we have performed a series
354 of rock magnetic analyses to fully characterize the magnetic mineralogy of the studied samples as a
355 step towards understanding the magnetization process and timing. We measured 18 high-field
356 thermomagnetic runs in an in-house-built horizontal translation-type Curie balance with a sensitivity
357 of approximately $5 \times 10^{-9} \text{ Am}^2$ (Mullender et al., 1993) and one in an AGICO KLY-3 susceptibility
358 bridge with a CS2 furnace attachment with nominal sensitivity (5×10^{-7} SI) and air forced into the
359 tube. This latter analysis included two heating and cooling cycles. We also analyzed 20 magnetic
360 hysteresis loops and one first order reversal curve (FORC) diagram. They were measured at room
361 temperature with an alternating gradient force magnetometer (MicroMag Model 2900 with 2 Tesla
362 magnet, Princeton Measurements Corporation, noise level $2 \times 10^{-9} \text{ Am}^2$). Finally, we obtained 88

363 isothermal remanent magnetization (IRM) acquisition curves from our Pyrenean limestone samples.
364 Curves were obtained with the robotized magnetometer system of Utrecht University (Mullender et
365 al., 2016).

366 Our paleomagnetic analyses were focused towards determining the Natural Remanent Magnetization
367 (NRM) of the rocks. NRM provides information about ancient latitudes (inclination of the magnetic
368 remanence) and rotations (declinations with respect to the past north) so that we can constrain the
369 magnetization timing. The NRM of the sample collection was investigated through alternating field
370 (AF) demagnetization and thermal demagnetization. AF demagnetization was carried out using the
371 aforementioned robotic 2G-SQUID magnetometer, through variable field increments (4–10 mT) up
372 to 70–100 mT. In all limestone samples, where high-coercitivity, low-blocking temperature minerals
373 (i.e. goethite, titano-hematite) were expected, a heating step to 150 °C was performed previous to the
374 AF demagnetization. At the same time this enhances the distinction between secondary and
375 characteristic NRM components determined with AF demagnetization (van Velzen & Zijdeveld,
376 1995). In samples demagnetized thermally, a stepwise thermal demagnetization was carried through
377 10–100 °C increments up to complete demagnetization. Principal component analysis (Kirschvink,
378 1980) was used to calculate magnetic component directions from orthogonal vector end-point
379 demagnetization diagrams (Zijderveld, 1967) with the online open-source software
380 Paleomagnetism.org (Koymans et al., 2016; 2020).

381 Anisotropy of magnetic susceptibility (AMS) measures the induced magnetization in a rock when
382 applying a magnetic field in different directions, defining an ellipsoid (e.g. Parés, 2015). The shape
383 of the AMS ellipsoid depends on the crystallographic preferred orientation of the minerals; the
384 shape, size, and preferred orientation of mineral grains; the occurrence of microfractures, its
385 distribution and size... Frequently it is a good proxy for sedimentary and tectonic fabrics that are

386 not visually obvious, but it is also a powerful method to investigate the effect of deformation on the
387 NRM. We determined the composite fabric of the paramagnetic, diamagnetic and ferromagnetic
388 grains by measuring the AMS of 148 samples from our collection with an AGICO MFK1-FA
389 susceptometer (nominal sensitivity 2×10^{-8} SI).

390 3.3 Rock magnetism results

391 3.3.1 Thermomagnetic analyses

392 We placed between 50–100 mg of powdered sample material from representative samples into
393 quartz glass cup holders that hold the sample with quartz wool. We programmed stepwise
394 thermomagnetic runs with intermittent cooling between successive heating steps. The heating and
395 cooling segments were 150, 100, 250, 200, 300, 250, 400, 350, 520, 450, 620, 550, 700° C and finally
396 back to 25° C, respectively. Heating and cooling rates were $10^\circ \text{C min}^{-1}$. Many samples show a
397 paramagnetic contribution, sometimes uniquely (OG19; Supplementary File SF1), sometimes with a
398 more or less noteworthy alteration reaction at about 400–450° C. This indicates the presence of
399 non-magnetic sulfides (likely pyrite) that oxidize to magnetite during the thermomagnetic run (Fig. 3;
400 OG14; Supplementary File SF1). Some samples show a small but sharp decay between 500 and 600°
401 C, indicating the presence of magnetite (Fig. 3, OG13), others show the presence of pyrrhotite with
402 a sudden increase at $\sim 300^\circ\text{--}320^\circ \text{C}$ followed by a sharp decrease afterwards (OG8 in Fig. 3; OG06
403 and OG07 in SF1). All samples showing pyrrhotite contained a less important, but observable,
404 content of pyrite. In the susceptibility vs. temperature curve (Fig. 3, BN1), pyrrhotite is observable
405 during cooling but it likely formed as a secondary mineral during one of the heating cycles.

406 3.3.2 Magnetic hysteresis

407 Representative samples with masses ranging from 20 to 50 mg were measured using a P1 phenolic
408 probe. Hysteresis loops were measured to determine the saturation magnetization (M_s), the
409 saturation remanent magnetization (M_{rs}), and the coercive force (B_c). These parameters were
410 determined after correcting for the paramagnetic contribution. The maximum applied field was 0.5
411 T. The field increment was 10 mT and the averaging time for each measurement was 0.15 s. We
412 found different loop shapes (Fig. 4, SF-2): (i) Loops that do not saturate at 0.5 T with a pseudo-
413 single-domain like shape which points to the presence of a relatively hard magnetic carrier likely
414 pyrrhotite (Fig. 4, OG08) and (ii) typical magnetite-like pseudo-single domain loops (Fig. 4, OG19).
415 We performed a first order reversal curve (FORC) diagram (Fig. 4, BN1-3) that shows a mixture
416 between superparamagnetic and single domain behaviour.

417 3.3.3 Isothermal Remanent Magnetization (IRM)

418 Before the actual IRM acquisition, samples were AF demagnetized with the static 3-axis AF protocol
419 with the final demagnetization axis parallel to the subsequent IRM acquisition field, a procedure that
420 generates IRM acquisition curves with a shape as close to a cumulative-lognormal distribution as
421 possible (Egli, 2004; Heslop et al., 2004). IRM acquisition curves consist of 61 IRM levels up to 700
422 mT. The shape of IRM curves is approximately a variably skewed cumulative log-Gaussian function
423 which may contain more than one coercivity phase. IRM component analysis enables a semi-
424 quantitative evaluation of different coercivity components (magnetic minerals or particle sizes) to a
425 measured IRM acquisition curve. Every skewed log-normal curve is characterized by four
426 parameters: (1) The field ($B_{1/2}$) corresponding to the field at which half of the saturation isothermal
427 remanent magnetization (SIRM) is reached; (2) the magnitude of the phase (M_{ri}), which indicates the
428 contribution of the component to the bulk IRM acquisition curve; (3) the dispersion parameter

429 (DP), expressing the width of the coercivity distribution of that mineral phase and corresponding to
430 one standard deviation of the log-normal function (Kruiver et al. 2001; Heslop et al. 2002); and (4)
431 the skewness of the gaussian curve (Maxbauer et al., 2016). IRM curve unmixing was performed
432 with IRM MaxUnmix package (Maxbauer et al., 2016). The interpretation of the coercivity
433 components in terms of mineralogy and grain size is usually done in concert with thermomagnetic
434 curves.

435 Results from individual samples are characterized by two main IRM components: (a) a relatively soft
436 component (C1 in Fig 5A) with $B_{1/2}$ between a minimum value of 23 and a maximum of 74 mT, but
437 generally ~ 40 mT and dispersion parameter (DP) of ~ 0.33 and 0.38 (log units); and (b) a high
438 coercivity component (C2) with a high $B_{1/2} > 200$ mT and DP ~ 0.5 (log units). Both components
439 are present in all samples but in varying proportions (Fig. 5A) of the SIRM. We performed end-
440 member modeling in all of the same lithology Silurian-Devonian samples (following the steps of
441 Gong et al. (2009a) but without a 150°C preheating of the samples) to fully characterize the IRM set
442 of samples. The program (Heslop and Dillon, 2007) to interpret the IRM acquisition curves uses the
443 algorithm developed by Weltje (1997). End-member modeling assumes that the measured data can
444 be represented by a linear mixture of a number of invariant constituent components, which are
445 referred to as endmembers. The algorithm dictates that input IRM acquisition curves are monotonic;
446 the curves were smoothed when appropriate to enforce them being monotonic. By least-squares
447 minimization calculated normative compositions are optimized to the measured IRM acquisition
448 curves, eliminating the need for prior knowledge of end-member properties (cf. Weltje, 1997). For
449 further information about this technique in the framework of remagnetization see the review by
450 Dekkers (2012). We found that a two end-member model shows an acceptable r^2 value of 0.6.
451 Models with 3 to 9 end members show slightly better fits ($r^2 = 0.73$ to 0.88 respectively) although
452 improvement is not deemed that significant (see discussion). The two end members are a soft (42

453 mT component with a DP = 0.36) and a hard (a 200mT component and DP = 0.35) component,
454 analogous to C1 and C2 in the individual IRM curves analyzed (Fig. 5C).

455 3.4 Paleomagnetism results

456 A minimum of five demagnetization steps was considered to characterize a remanent component. In
457 specimens where directions were difficult to isolate, we used the approach of McFadden and
458 McElhinny (1988) in combining great circles and linear best fits (set points). The Virtual
459 Paleomagnetic Directions (VPD) software was also used (Ramón et al., 2017) at the site level
460 (stacking routine, linearity spectrum analysis, and the virtual direction methods by Scheepers and
461 Zijderfeld (1992); Schmidt (1982) and Pueyo (2000), respectively) to confirm the means derived
462 from PCA analyses of individual specimens. Representative Zijderfeld diagrams are shown in Fig. 6.
463 For the complete analyses, the reader can check the paleomagnetism.org files associated with this
464 paper (check persistent identifier -PID- in the acknowledgements) and Supplementary File SF3.

465 Mean directions and uncertainties of each component were evaluated using Fisher's statistics (1953)
466 of virtual geomagnetic poles (VGPs). We applied a fixed 45° cut-off to the VGP distributions of
467 each site. In addition, we used the Deenen et al. (2011) criteria to evaluate the scatter of VGPs. As a
468 general rule, if scatter is—mostly—due to paleosecular variation (PSV) of the geomagnetic field, the
469 associated VGP distribution is roughly circular in shape. However, internal deformation, vertical axis
470 rotation or inclination shallowing may add anisotropy to the scatter. In such cases, VGP
471 distributions will show a certain degree of elongation or are otherwise not spherically uniform. Many
472 samples show a NRM component with very low unblocking temperatures and low coercivities (100–
473 180 °C or 10–12 mT). We consider this component as a viscous remanent magnetization (VRM),
474 because of its similarity to the recent field (Fig. 7 and Supplementary File SF3-A and B).

475 After VRM removal, the samples show a single NRM component (Fig. 6), generally trending to the
476 origin, regardless of the mineral, magnetite (usually fully demagnetized at 40-60 mT and 500-580° C)
477 and/or pyrrhotite (fully demagnetized at 330° C and little to barely demagnetized in AF). This
478 characteristic remanent magnetization (ChRM) clusters well in all the sites (concentration parameter
479 $k > 8$, but generally over 15; Table 2; Supplementary file SF3-B) with the exceptions of sites OG02
480 and OG08 (Figs. 8 and 9; Table 2). In addition, there are three sites with less than seven samples
481 passing the 45° cut-off (OG05, OG06, OG14) and therefore their statistical parameters are not
482 reliable. These five sites were excluded from further interpretation. The remaining 15 sites show
483 quite variable ChRM declinations and inclinations which appear to be only comparable between sites
484 within the same thrust unit (Figs. 2, 8 and 9, Tables 1 and 2). To account for the different events of
485 deformation we have used bedding corrections (Table 2) and fold tests (Fig. 10). In addition, we also
486 performed inclination only statistics (Enkin and Watson, 1996; Arason and Levi, 2010) to eliminate
487 clustering problems related to vertical axis rotations using both the bedding parameters and our
488 inferred Alpine corrections (see top of section 3) (Tables 1 and 3).

489 In geographic coordinates sites that passed the quality filter show clusterings that range from k
490 (concentration parameter) ~ 8 (OG10 and 11) to $k \sim 188$ (OG19). Site average declinations range
491 from 125° to 297°, the majority of them in the south quadrants with sites OG15 and BN1-OR15
492 (combined sites separated by 100 m) being the only exceptions (Fig. 8 and 9; Table 2). Inclinations
493 range from -50° to 50°. Bedding correction significantly changes the distribution of the site averages,
494 but the scattering in declinations (from 111° to 289°) and inclinations (-65° to 56°) remains (Table
495 2), which means that magnetization timing is not the same for all samples and/or structural
496 complications are larger than folding.

497 All fold-tests whose samples passed the aforementioned quality criteria (Fig. 10; OG03-04; OG11;
498 OG13 and OG19) were performed in folds with weakly plunging axes (Table 1; Fig. 11) with the
499 exception of OG11, which in turn is the only one that is not negative (Fig. 10). OG11 shows a
500 better clustering (τ_1) after tilt correction, however, the fold-axis in site OG11 is steeply plunging (the
501 only case; Fig. 10). The performed fold-tests restore deformation as if axes were horizontal. Steeply
502 plunging axis' folds, therefore usually yield false positives and negative foldtests (e.g. Pueyo et al.,
503 2016a). A possibility to decipher the magnetization timing is pre-correcting the plunge of the fold
504 axis before the fold-test. The declination results, in this case, will bring spurious rotations and
505 wouldn't be trustworthy. After back-tilting the plunging-axis in OG11 (azimuth/plunge = 005/42),
506 the fold test remains indeterminate, in this case with a greater clustering (τ_1) before tilt correction
507 (Figs. 10 (structural correction panel) and 11). The statistics of all sites that pass our quality criteria
508 ($n \geq 7$ and $k > 8$) yield close to random distributions both considering all specimens ($k = 1.63$ and
509 $K = 1.65$; Supplementary File SF3-A) and the mean of site averages ($k = 1.95$ and $K = 2.5$; Table 4).
510 As expected from the negative within-site fold-tests, the concentration parameter does not change
511 after bedding correction neither in all specimens together ($k = 1.51$ and $K = 1.59$; Supplementary
512 File SF3) nor the mean of site averages ($k = 1.57$ and $K = 1.64$; Table 4).

513 Inclination only statistics are independent to differential vertical axis rotations since declinations are
514 not taken into account (e.g. Enkin and Watson, 1996). Inclination only statistics were performed on
515 site averages to avoid weighting based on number of specimens (Table 4). The concentration
516 parameter (k) equals to 0 in geographic coordinates and 2.17 in tilt corrected coordinates, both
517 figures representing very poor clusterings. k becomes close to 4 if we do not account for OG3 and
518 OG4, which follow a different trajectory and may represent a different magnetization event (see
519 explanation below). In contrast, when correcting the studied samples exclusively for our inferred

520 Alpine tilt, the inclination only concentration parameter is ~ 4 , but becomes ~ 14 when excluding
521 OG3 and OG4 (Table 4). An inclination only tilt test without OG3 and OG4 shows a best fit for a
522 110% correction, both using the Enkin and Watson, 1996 approach (with a maximum clustering
523 around $k \sim 12$) and a stepwise untilting following Arason and Levi (2010) inclination only statistics
524 with a maximum at $k \sim 15$ (Fig. 12). OG3 and OG4 share a common true direction in geographic
525 coordinates and their Alpine tilt correction does not change them too much (Fig. 13)

526 3.5 Anisotropy of the Magnetic Susceptibility (AMS) results

527 We measured the anisotropy of the magnetic susceptibility in 148 samples from most sites to
528 explore possible causes for the variety of ChRM directions found (Table 2). The degree of
529 anisotropy (P) appears to be generally low (< 1.05 ; Fig. 14, Supplementary file SF5) although some
530 individual samples showed up to 1.5. The samples' three principal ellipsoid axes (K_{max} , K_{int} , and
531 K_{min}) mimic the bedding (S_0 , K_{max} - K_{int} fall within the bedding plane and K_{min} is perpendicular)
532 in six sites (OG09, 15, 16, 17, 18, 19); in three samples the AMS ellipsoid corresponded to the
533 foliation S_1 (OG06, 10 and 13); and others showed a quasi-random pattern (OG03, 05, 11, 14) both
534 in geographic and tectonic coordinates (Fig. 14). No observed AMS fabric (not K_{max} , K_{int} , or
535 K_{min} axes) from the datasets studied coincides with the ChRM directions, suggesting that NRM and
536 ChRM are not significantly biased by rock fabric.

537

538 4. Discussion

539 The paleomagnetic and rock magnetic results obtained from the Silurian-Devonian limestones in the
540 Pyrenees certify that the Paleozoic rocks from this mountain belt have been subject to at least one

541 widespread remagnetization event. Many samples contain a VRM that is similar to the recent
542 geoaixial dipole for recent times in the Pyrenees (Fig. 7). Apart from this VRM, all rocks, regardless
543 of their magnetic mineralogy, show a single stable component heading to the origin, with the
544 exception of samples not delivering results (Fig. 6 and 8). This component is not deviated toward
545 bedding/cleavage planes (as inferred from AMS patterns, Fig. 14) and displays negative fold tests
546 (Fig. 10; perhaps a syn-folding remagnetization in the case of site OG11 where fold test results are
547 indeterminate).

548 4.1 Rock magnetism

549 Rock magnetic analyses show that both pyrrhotite and magnetite are the magnetic carriers in the
550 Silurian-Devonian limestones whereas magnetite is the carrier in the Panticosa late Carboniferous-
551 Permian granite (OG1) and sampled dyke (OG12dyke). All limestone sites contain variable amounts
552 of pyrrhotite and magnetite as shown both in thermomagnetic curves (Fig. 3), in IRM acquisition
553 curves and during NRM demagnetization (Figs. 5 and 6). We applied the IRM end-member
554 modeling technique in an attempt to discriminate between different remagnetization events in the
555 Pyrenees. The two end-member model with a reasonably high r^2 value of 0.65 is our preferred
556 model. Models with 3 to 9 end members evidently show slightly better fits ($r^2 = 0.73$ to 0.88
557 respectively). However, neither the fit improves significantly, nor the shape of the end members
558 shows more or less anticipated IRM acquisition curves for any particular mineralogy (Fig. 5B). In
559 addition, most of the additional end members seem to represent the variable coercivity windows of
560 magnetite (e.g. the 4 endmember solution in Fig. 5B: three of the endmembers (EM1-3) represent
561 magnetite and do not deliver any particular meaningful result). All samples contain a significant
562 amount of those additional endmembers (varying from 10% to 60%) indicating that a variable grain-
563 size or compositional (Ti-)magnetite is present in virtually every sample. The two end-member

564 model further distinguishes a 42 mT component with a DP = 0.36 (C1), which is typical for
565 magnetite and a 200mT component and DP = 0.35 (C2), which we interpret as pyrrhotite (Fig. 5C).
566 The two end members are in agreement with individual sample fits, but end-member IRM
567 acquisition curves describe much better the IRM properties of each magnetic phase (Fig. 5). We
568 interpret the soft component (C1) as magnetite varying from coarse to very fine grained (i.e. lower
569 and higher coercivity respectively) as supported by hysteresis loops (Fig. 4 and SF2). It is reasonable
570 that the high coercivity component (C2) reflects the observed pyrrhotite in the thermomagnetic
571 curves as SD pyrrhotite has a rather high coercivity (Dekkers, 1989).

572 The presence of variable amounts of pyrrhotite and magnetite in all Silurian-Devonian samples
573 studied suggests that this is a common feature for the Paleozoic sedimentary and metasedimentary
574 units of the mountain belt. Similar to the Pyrenees, pyrrhotite is the most common magnetic carrier
575 in other limestone formations of the Iberian Variscides heavily affected by late Carboniferous
576 magmatism (Pastor-Galán et al., 2015a; 2016; 2017; Fernández-Lozano et al., 2016).

577 In general terms, the occurrence of pyrrhotite in limestones is a sign of their remagnetization.
578 Pyrrhotite is a frequent secondary mineral which is formed in low-grade metamorphic rocks under
579 reducing conditions (Crouzet et al., 2001; Aubourg et al., 2012, 2019; Izquierdo-Llavall et al., 2020)
580 or in the presence of non oxidizing magmatic fluids (Pastor-Galán et al., 2016). The occurrence of
581 pyrrhotite has been used as a geothermometer; increasing burial enhances the transformation of
582 magnetite to pyrrhotite and the progressive replacement of magnetite-carried magnetizations by
583 pyrrhotite-carried remagnetizations (e.g. Aubourg et al., 2019). In clay-rich rocks, magnetite and
584 pyrrhotite coexist at burial temperatures <340 °C whereas at ~350 °C the concentration of
585 magnetite decreases drastically and pyrrhotite becomes the dominant magnetic mineral (Aubourg et
586 al., 2019). Izquierdo-Llavall et al. (2020) estimated the peak temperatures (~350 – 450 °C) in the

587 North Pyrenean Zone (between the northernmost sides of cross sections 2a and 2b in Fig. 1)
588 following the magnetite –pyrrhotite transformations. In contrast, the temperature estimates for the
589 sampled area, in the southern Pyrenees (Izquierdo-Llavall et al., 2013; Labaume et al., 2016) are
590 much lower (below ~ 300 °C) and the burial/thermal effect in the formation of pyrrhotite is
591 expected to be less important. Taking that into account, we suggest that in our samples pyrrhotite
592 could be mainly formed by a fluid induced chemical remagnetization during the latest stages of the
593 Variscan orogeny. However, our westernmost sampled units (OG1-OG4) may have surpassed the
594 Curie temperature of pyrrhotite (~ 320 °C; e.g. Dekkers, 1989) during the Cenozoic burial (Bosch et
595 al., 2016), and could, therefore, carry a Cenozoic TRM.

596 In pyrrhotite, the magnetic easy direction is confined to the basal crystallographic plane which
597 implies an intrinsically strong anisotropy because of the ‘hard’ crystallographic c-axis (Schwarz and
598 Vaughan, 1972; Schwarz, 1974). When pyrrhotite grows oriented in a preferred fabric (e.g. S1 or S0),
599 the direction of the magnetic remanence can be biased towards the fabric plane (Fuller, 1963). The
600 studied samples occasionally show pressure solution cleavage and a widespread presence of
601 pyrrhotite as a partial or main carrier of the NRM. AMS fabrics revealed that pyrrhotite is not
602 oriented according to the S1 fabric, and therefore preclude major biases in the magnetic remanence
603 of such secondary sulfides. Besides, although our AMS results are frequently consistent with bedding
604 (S0), the magnetic remanence is not contained within bedding planes (Fig. 14; Table 2) which also
605 impedes a deviation of the ChRM towards S0.

606 4.2 Paleomagnetism and timing of remagnetization

607 We only considered sites for interpretation with at least 7 specimens passing the VGP’s 45° cut-off
608 criterion and with the concentration parameter $k > 8$. Sites OG02, 05, 06, 08, 14 and the dyke in
609 OG12 do not pass these criteria and are not considered for further interpretation (Table 2). The rest

610 of the sites show k values that range from barely above 8 in geographic coordinates (OG10 and 11),
611 which could be expected also from detrital magnetizations, to over 40 (OG12, OG15, OG17-
612 OG19) in geographic coordinates, which is unlikely in primary magnetizations of sediments (e.g.,
613 Deenen et al., 2011). Site averages point generally to ESE-WSW with both positive and negative
614 inclinations in geographic coordinates with the only exceptions of OG15 and BN1-OR15 which
615 point WNW (Fig. 8 and 9; Table 2), something that does not change after bedding correction. With
616 the exception of OG11, we have documented post-folding magnetizations. Importantly, the fabrics
617 do not show consistency with NRM directions (AMS fabric coincident with S1 does not occur and
618 ChRMs are not within bedding planes) suggesting that any potential bias caused by a preferred
619 orientation of pyrrhotite particles is not significant. Therefore, a post Variscan folding (i.e. late
620 Carboniferous) is the oldest possible age for the magnetization since no earlier folding event has
621 been described in the Pyrenees. The OG11 fold, which has a steep plunging axis (Fig. 11), yielded an
622 inconclusive fold-test, but shows better clustering after tilt correction (Fig. 10). Classical fold-tests
623 assume horizontal axes and performing them in steeply plunging axis' folds is unreliable (e.g. Pueyo
624 et al., 2016a) In the case of OG11, pre-correcting the fold axis plunge produces another inconclusive
625 result (Fig. 10). However, declinations in geographic, standard bedding correction, and Alpine tilt
626 correction remain around 200° (Table 2 and 3) and inclinations are in all cases relatively shallow
627 (between -9 and 20), suggesting that OG11 acquired its NRM during a reversed chron during a time
628 when Iberia was at equatorial latitude: during late Carboniferous or Permian times regardless of the
629 result of the foldtest (e.g. Pastor-Galán et al., 2018).

630 When considering all site paleomagnetic directions, we found that declinations and inclinations are
631 only compatible in geographic coordinates for those sites within the same tectonic unit (Figs. 1, 2, 8,
632 9; Table 2). Such a directional pattern may be indicative of (a) different timing of NRM acquisition
633 for each tectonic unit, (b) differential vertical axis rotations between units, (c) post-magnetization

634 differential tilting between units or (d) a combination of the previous processes. To distinguish
635 between these options inclination only statistics are appropriate (e.g. Enkin and Watson, 1996).
636 Inclination only statistics do not consider declinations and therefore are independent of variations
637 due to differential vertical axis rotations. In order to evaluate potential timing of magnetization we
638 performed statistical analyses in geographic coordinates, after bedding correction, and also after
639 correction of the tilt related to the emplacement of Alpine basement thrusts (Figs. 2, 12, 13; Tables 3
640 and 4). The concentration parameter of inclination data (k) is 0 in geographic coordinates (Table 4),
641 which could mean that (i) sites magnetized at significantly different geological times when Iberia was
642 at very different latitudes, and/or (ii) Alpine tilting postdates the magnetization and therefore it has a
643 strong influence on the inclinations. Inclination only k is still too low (minimum $k \sim 8$ to consider
644 an acceptable clustering) after bedding correction (~ 2) but also after Alpine tilt correction (~ 4).

645 Two sites from the Gavarnie thrust unit (OG03 and OG04; Fig. 8 and 13, geographic coordinates)
646 move in a very different direction both during bedding and Alpine tilt corrections. In contrast,
647 OG01 (Panticosa granite, late Carboniferous-Permian, Denèle et al., 2012), which is in the same
648 Gavarnie thrust unit, correlates well with the rest of the sites in all thrust units after Alpine tilt
649 correction but not with the neighboring OG03 and OG04. Thus, those sites might have acquired
650 their magnetization at a significantly different time than the rest. After removing OG03 and OG04,
651 the inclination only concentration parameter still indicates poor clustering after bedding correction
652 ($k \sim 4$). However, when correcting only for the Alpine tilt k becomes 14.42 and a positive
653 inclination only tilt test with a maximum in a 110% untilting is obtained (95% between 58 and 150;
654 Fig. 12; Table 4). After the Alpine tilt correction, the mean inclination is $5^\circ \pm 11$ (Table 4) and all
655 included sites show SW to SE declinations (Fig. 12). Despite the positive result, our Alpine tilt
656 correction should be taken cautiously. We considered only regional tilt values, which were inferred
657 from the average orientation of the overlying Mesozoic units and thrust slopes in geological maps

658 and cross-sections (Fig. 2). Our estimated values took into account the kilometric-scale, thrust-
659 related folding of the basement but can not consider the potential contribution of Alpine, outcrop-
660 scale folding of the Paleozoic strata.

661 We believe, however, that the inclination only k value of 14.42 together with the obtained shallow
662 inclinations and southerly declinations are sufficiently convincing to argue for a common timing of
663 NRM acquisition for the samples included in the tilt test (Fig. 12). The results imply a postfolding
664 but a pre-Alpine tilt NRM. The shallow inclinations suggest that Iberia was located at equatorial
665 latitudes and the southerly declinations suggest that this occurred during a reverse chron. We
666 therefore suggest that all samples that passed the quality criteria, with the exception of sites OG03
667 and OG04, magnetized during the latest Carboniferous to middle Permian times during the Kiaman
668 reverse superchron, when Iberia was indeed located at equatorial latitudes (Weil et al., 2010). The
669 late Carboniferous and early Permian times in the Pyrenees are characterized by widespread
670 intrusions and volcanism (Panticosa granite, for example, OG01; Gleizes et al., 1998). We
671 hypothesize that the remagnetization mechanism in the Pyrenees was triggered by fluids associated
672 to the magmatic activity analogously to the remagnetizations observed in the Central Iberian Zone
673 of west Iberia (e.g. Fernández-Lozano et al., 2016; Pastor-Galán et al., 2016; 2017).

674 To further test the hypothesis of a post-Variscan but pre-Alpine orogeny remagnetization with the
675 exception of OG03 and OG04, we have plotted the paleolatitudes and declinations of OG sites
676 compared to the Global Apparent Polar Wander Path (GAPWaP) of Torsvik et al. (2012) rotated to
677 Iberian coordinates (Pastor-Galán et al., 2018). Paleolatitudes of OG sites show a good fit and
678 variable clockwise rotations with respect to the declinations expected in Iberia for Carboniferous
679 and early Permian times after Alpine tilt correction, with the exception of OG03 and 04 (Fig. 15 A).
680 Whereas, both paleolatitudes and declinations are scattered in geographic coordinates, in contrast to

681 the expected general good fit if remagnetization had happened after the Alpine orogeny, when Iberia
682 was tectonically stable (Fig. 15 B). In geographic coordinates only three sites fit in both paleolatitude
683 and declinations with the post-Alpine GAPWaP segment: OG3, OG4, and OG16. However, we
684 interpret OG16 as a Permian remagnetization since it fits much better with its neighboring sites
685 OG17, 18 and 19 after the correction of the alpine tilt.

686 OG03 and OG04 show a negative fold test (Fig. 10) and a common true mean direction in
687 geographic coordinates (Fig. 13). Their paleomagnetic direction is, however, significantly different
688 from OG01 that is a late Carboniferous-early Permian site located in the same thrust sheet. OG03
689 and OG04 show declinations to the south (both in geographic coordinates and after Alpine tilt
690 correction) and upward inclinations of -43° and -48° (geographic coordinates) or -60° and -68° (after
691 the restoration of the inferred Alpine tilt respectively). Both geographic and Alpine tilt corrected
692 data indicate a remagnetization when Iberia was located at latitudes between 25° and 50° during a
693 reverse chron (Fig. 15A, B). OG03 and 04 results fit best with a remagnetization that postdates the
694 Cretaceous normal superchron (e.g. Izquierdo-Llavall et al., 2015 and references therein) (Fig. 15).
695 Inclinations $>60^\circ$ (i.e. after Alpine tilt corrections) would only be possible when Iberia was located
696 at similar latitudes as at present, fairly long after the Alpine orogeny which ended at Miocene times.
697 In such case, no correction at all should be applied. Therefore, the magnetization has to be syn- to
698 post Alpine tilting to achieve a good paleolatitudinal fit. Most structural units just above the
699 basement units are remagnetized by tardi-orogenic burial remagnetizations (post-, syn- and pre-
700 Alpine folding) that affected all kinds of rocks (limestones, calcarenites, redbeds...) (Dinarès et al.,
701 1992; Dinarès, 1994; Keller et al., 1994; Oliva-Urcia and Pueyo, 2007b; Izquierdo-Llavall et al., 2015,
702 Mujal et al., 2017 etc.) In addition, the burial temperature of OG03 and OG04 could have been
703 sufficiently elevated to trigger a thermal remagnetization after tilting during the unroofing and
704 exhumation of the Axial Zone. With all this elements, we tentatively favor a late orogenic (Eocene)

705 age which would allow inclinations around 50° (close to those obtained in geographic coordinates;
706 Fig. 15B).

707 4.3 Tectonic significance

708 The hypothesis of a detachment and northward drift of a peri-Gondwana microcontinent (Armorica
709 s.l.) during the late Silurian or early Devonian (e.g. Torsvik et al., 2012; Stampfli et al., 2013;
710 Domeier and Torsvik., 2014; Franke et al., 2017) is grounded largely on the basis of paleomagnetic
711 data from the Silurian and Devonian rocks of the Pyrenees (Tait et al., 2000), Brittany (Tait et al.,
712 1999) and Bohemian Massif (Tait et al., 1994). Our results show that pervasive remagnetizations
713 have affected the Silurian-Devonian limestones of the Pyrenees during, at least, two episodes: late
714 Carboniferous-Early Permian and at the end of the Alpine orogeny. Our site BN1-OR15 was
715 collected in the vicinity of those from Tait et al. (2000) and shows the same direction in geographic
716 coordinates (Fig. 9), but within-site clustering worsens after bedding correction (Table 2). After
717 Alpine tilt correction, however, a very good fit results with the majority of our Silurian-Devonian
718 collection. In addition, site BN1-OR15 contains pyrrhotite (Fig. 3), a feature common to all the
719 other samples studied (Fig. 9) and a secondary mineral in (meta)sediments indicative of
720 remagnetization (e.g. Pastor-Galán et al., 2017; Izquierdo-Llavall et al., 2020). We therefore conclude
721 that the originally published data by Tait et al. (2000) also reflect a remagnetization. Since the other
722 paleomagnetic results from the putative Armorican s.l. continent are similar to those from the
723 Pyrenees and come from areas with intense Carboniferous deformation and enhanced thermal
724 activity, we suspect that they could be remagnetized as well. We request using those paleolatitudes
725 (Tait et al., 1994; 1999) with caution; their paleomagnetic veracity warrants to be reassessed.

726 Despite the inherent loss of information due to the remagnetization, especially regarding the
727 potential paleolatitudinal constraints, the Silurian-Devonian rocks of the Pyrenees do provide

728 interesting insights. Based on the inclination data we interpret that the sampled rocks mostly
729 remagnetized during late Carboniferous and Permian times when Iberia was located around the
730 equator, thus previous to the Alpine orogeny. Our paleomagnetic results show a positive inclination
731 only fold test when correcting the Alpine tilt inferred from cross-sections and geological maps but
732 negative outcrop scale fold tests when using the bedding parameters. Thus, paleomagnetism in
733 combination with detailed structural analysis, is a reliable tool to unravel the deformation style of
734 multi-phase orogens like the Pyrenees. With our paleomagnetic data we now can separate the effects
735 of Alpine and Variscan orogeny in the Silurian-Devonian carbonate series, something that classically
736 is deemed challenging (e.g. Casas et al., 2019). With our data we can say that the Variscan orogeny
737 was responsible for the main folding event observed in the Silurian and Devonian rocks since all
738 remagnetizations are post-folding (Figs. 10 and 12).

739 After the Alpine tilt correction, we obtained a relatively good agreement in inclinations, but
740 declinations are still really scattered from SE to SW. Alpine vertical axis rotations in the Pyrenees are
741 frequent and very variable with magnitudes ranging from a few degrees to up to 80° both clockwise
742 and counterclockwise (e.g. Sussman et al., 2004; Rodríguez et al., 2016). Although it is plausible that
743 the basement also underwent significant vertical axis rotations, very little is known about the
744 rotational activity of Pyrenean basement thrusts during the Alpine orogeny. The declinations
745 observed in the Silurian-Devonian rocks of the Pyrenees are generally clockwise rotated with respect
746 to the Permian reference pole for stable Iberia (Weil et al., 2010; Oliva et al., 2012): These rotations
747 range from a few degrees to ca. 90° (Fig. 1). We note that such results are also in line with the
748 paleomagnetic results from Carboniferous and Permian igneous rocks in the Pyrenees and Catalan
749 coastal ranges (Edel et al., 2018). The Pyrenees lay in the northern branch of the Cantabrian
750 Orocline, which rotated clockwise during the Late Carboniferous and Early Permian (e.g. Pastor-
751 Galán et al., 2015b; Pastor-Galán, 2020). Edel et al. (2018) interpreted their results as consistent with

752 the rotations expected in the northern branch of the Cantabrian Orocline. Izquierdo-Llavall et al.
753 (2014) also found similar data in late Carboniferous and Early Permian rocks of the Pyrenees and
754 interpreted them as an Alpine rotation. We would like to remain wary about their meaning since the
755 variety of rotations found might be reflecting: (i) Differential timing of the remagnetization which
756 occurred widely during the Cantabrian Orocline formation as observed in other areas of Iberia (e.g.
757 Pastor-Galán et al., 2017; 2020); (ii) Vertical axis rotations associated with the Alpine orogeny
758 (Izquierdo-Llavall et al., 2014); or (iii) a combination of both processes where the Alpine rotations
759 may be opposite to and/or in the same sense as the late Carboniferous clockwise rotations (Fig. 15).

760 4.4 A blessing in disguise

761 The Pyrenees are a multi-orogenic mountain range whose kinematics is often complicated due to the
762 superposition of different deformation events. Accumulation of geological processes, many of them
763 involving relatively high temperatures and fluid percolation increases the chances of remagnetization
764 for the rocks involved in the orogenies. In fact, we suspect that the majority of the Silurian-
765 Devonian carbonate series of the Pyrenees won't preserve any primary and syn-sedimentary
766 magnetization. This makes the Pyrenees, despite the great outcrop quality and quantity, a bad
767 candidate to study pre-Variscan plate motions and kinematics. However, we found generally strong
768 magnetizations containing univocal ChRMs, which makes paleomagnetism of Paleozoic series in the
769 Pyrenees useful for post-Variscan tectonic studies. Our paleomagnetic data, in combination with
770 detailed structural observations, has proven an efficient way to unravel the complex tectonic
771 evolution of the Axial Zone of the Pyrenees. We think that at least the Silurian-Devonian carbonate
772 rocks, but likely other Paleozoic series and igneous rocks are excellent targets to study: (1) the
773 Variscan - Alpine structural relationships, (2) the Alpine rotational history of the basement thrusts;
774 and, perhaps, (3) the late Variscan deformation events leading to the final amalgamation of Pangea.

775 5. Conclusions and caution for paleomagnetists

- 776 • The Silurian-Devonian carbonate series of the Pyrenees show varying amounts of pyrrhotite,
777 a secondary magnetic mineral, and negative fold tests using bedding parameters, which
778 indicate widespread remagnetization(s).
- 779 • The majority of sites that passed the quality criteria ($n \geq 7$ and $k > 8$) show a positive
780 inclination only fold test when correcting the alpine tilt (with the exceptions of OG03 and
781 OG04). The obtained inclinations are southerly and very shallow, constraining the
782 remagnetization to a reverse chron when Iberia was around the equator, only possible during
783 late Carboniferous or early Permian times.
- 784 • Sites OG03 and OG04 (Western Axial Zone, Gavarnie thrust sheet) were likely
785 remagnetized after the main Alpine thrusting, during a pervasive burial remagnetization
786 widely observed in the Internal Sierras and other along-strike equivalent units (Bóixols,
787 Cadí).
- 788 • Paleomagnetism from the Silurian and Devonian rocks suggests that the Variscan orogeny
789 was responsible for their main folding event, whereas the Alpine orogeny produced their
790 thrusting and antiformal stacking.
- 791 • Our results also show general clockwise rotations which may be consistent with the northern
792 branch of the Cantabrian Orocline. These rotations may as well represent Alpine vertical axis
793 rotations or a combination of both.
- 794 • Given the generally good paleomagnetic quality of the Devonian carbonates, they could be
795 targeted to study the Alpine imprint on Paleozoic rocks and thus, to unravel the rotational
796 history of basement thrusts.

- 797 • The widespread remagnetizations found in the Paleozoic of the Pyrenees indicate that
798 paleolatitudes inferred for Silurian and Devonian times from the studied rocks are very
799 unlikely original and should be taken very cautiously. We urge a reassessment of Siluro-
800 Devonian poles from the Variscan in Europe.
- 801 • Paleomagnetism from multi-orogenic areas is NOT A SIMPLE GAME. However, the
802 systematic combination of paleomagnetism with detailed structural observations, seems to
803 be a foremost way to unravel complex tectonic evolutions.

804

805 **Acknowledgements**

806 We really thank the reviewers, Augusto Rapallini and Roberto Molina-Garza for their thorough,
807 positive and very constructive reviews, which in turn made of our work a much better one. This
808 work was funded by postdoctoral (ISES) grant from NWO to DPG and the projects DR3AM,
809 MAGIBER II and UKRIA4D (CGL2014-54118-C2-2, CGL2017-90632-REDT and PID2019-
810 104693GB-I00/CTA) from the Spanish Ministry of Science. We thank Mat Domeier for
811 providing help with the inclination only statistics. DPG thanks Edward Lodewijk Van Halen for
812 all times making him jump, we will keep on jumping.

813

814 **Data availability statement**

815 All data is included in the paper and supplementary materials. In Addition, paleomagnetic data is
816 stored in paleomagnetism.org under the persisitent identifier (PID)

817 1871091757a6ef9d46ac59bb9f35c7a6387bc8fcede7bf0715eaba29164fbc7e and can be accessed
818 in the link <https://www.paleomagnetism.org/library/>.

819 **Figure and Table captions**

820 Figure 1: A) Simplified map of the Iberian Peninsula showing the main Paleozoic outcrops and
821 the areas affected by the Alpine orogeny (after Pastor-Galán et al., 2020). B) Geological map of
822 the Pyrenees (modified from Barnolas et al., 2008 according to Choukroune and Seguret, 1973)
823 showing our sampling locations (red dots) and the extensive paleomagnetic studies in the
824 Pyrenees focused mainly on Permo-Triassic rocks (blue dots). Lines show the trend of the cross
825 sections in figure 2.

826 Figure 2: Cross sections through the Pyrenees with projected positions of our sampling sites. The
827 cross-section in a) is from Teixell (1996) whereas cross-sections in b) and c) are from Martínez-
828 Peña and Casas-Sainz (2003) and Muñoz (1992), respectively.

829 Figure 3: Selected magnetization vs. temperature curves (OG8, OG13, OG14) and susceptibility
830 vs. temperature (BN1). Note that magnetic and non magnetic sulfides are common. All
831 measurements performed are available in supplementary file SF1.

832 Figure 4: Selected slope corrected hysteresis loops and FORC diagram (plotted with FORCINEL
833 (Harrison and Feinberg, 2008, smoothing factor 13). All measurements performed are available
834 in supplementary file SF2.

835 Figure 5: A) Unmixing of IRM acquisition curve for three samples showing different proportions
836 of a ‘soft’ mineral that saturates below 75 mT (magnetite) and a ‘harder’ one that saturates over
837 200 mT (pyrrhotite). B) Results from the endmember modeling showing our preferred two end-

838 member solution (left) and the four end-member solution (right). C) Unmixing of the IRM
839 synthetic acquisition curve from the two end members showing the same two magnetic
840 mineralogies as in the forward modeling of different samples: magnetite to the left and pyrrhotite
841 to the right.

842 Figure 6: Examples of 'Zijderveld' vector-end point plots (Zijderveld, 1967) for selected
843 samples. All samples plotted in geographic coordinates. Close-open circles represent declination
844 and inclination projections respectively. Complete analyses are available in paleomagnetism.org
845 through the Persistent identifier PID given in the acknowledgements.

846 Figure 7: Viscous remanent magnetization (VRM) from all samples is compatible with the
847 present-day field (geographic coordinates). Red dots are those that fall outside of the 45° cut-off.
848 Uncertainty envelope is in both cases VGP A95. The rather large scattering is likely due to the
849 small number of demagnetization levels containing the VRM (3-4) and the possible migration of
850 the VRM during transport, storage and analysis.

851 Figure 8: Directional and VGP results in geographic coordinates of sites OG01 to OG11.
852 Uncertainty envelope is in both cases VGP A95. Red dots are those that fall outside of the 45°
853 cut-off. Sites OG02, 05 and 08 did not provide statistically meaningful results and were not
854 interpreted.

855 Figure 9: Directional and VGP results in geographic coordinates of sites OG12 to OG19 and
856 BN1-OR15. Uncertainty envelope is in both cases VGP A95. Red dots are those that fall outside
857 of the 45° cut-off. Sites OG02, 05 and 08 did not provide statistically meaningful results and
858 were not interpreted.

859 Figure 10: Within-site fold tests. All are negative but OG11, which is inconclusive.

860 Figure 11: Pi diagrams for the studied folds. Only OG11 shows a steeply plunging axis.

861 Figure 12: Results after the inferred Alpine tilt correction. Permian reference declination for
862 Iberia is after Weil et al. (2010). The results show a positive inclination only tilt test following
863 the methodology of Enkin and Watson (1996) (selected bootstraps in thin gray lines) and Arson
864 and Levi (2010) approach (dashed line).

865 Figure 13: OG03 and OG04 show a common true mean bootstrapped direction (after Tauxe,
866 2010) in geographic coordinates (and Alpine tilt corrected, since it is the same for both).

867 Figure 14: Results from the anisotropy of the magnetic susceptibility analyses. Magnetic fabrics
868 represent bedding or S1 cleavage. Magnetic fabric directions do not coincide with the
869 paleomagnetic directions, which allows us to discard an internal deformation control of the
870 paleomagnetic remanence.

871 Figure 15: Figure showing paleolatitudes (up) and declinations (down) of OG sites compared to
872 the GAPWaP of Torsvik et al. (2012) rotated to Iberia (following Pastor-Galán et al., 2018). A)
873 After Alpine Tilt B) Geographic coordinates.

874 Table 1: Site Location and key structural data from each site.

875 Table 2: Paleomagnetic results for ChRM component for all sites in geographic and tilt (bedding)
876 corrected coordinates.

877 Table 3: Paleomagnetic results (ChRM) after the Alpine tilt correction (tilt associated to the
878 emplacement of the thrusts).

879 Table 4: Concentration parameters of inclination only statistics from the mean values of the sites.

880 Supplementary Files:

881 SF1: All thermomagnetic curves analyzed.

882 SF2: All Hysteresis loops analyzed.

883 SF3: A) Synthesis of the paleomagnetic results (can be opened with paleomagnetism.org). B)

884 Extra plots and table showing the mean VRM per site and the mean ChRM per site in tectonic
885 coordinates.

886 SF4: KMZ file (Google Earth) with the sampled locations.

887 SF5: Graphics showing all results of the AMS analyses.

888 SF6: Zip file containing all obtained raw results.

889 **References added by Emilio, Esther and Jaume**

890 Abd Elmola, A., Buatier, M., Monié, P., Labaume, P., Trap, P., & Charpentier, D. (2018). $^{40}\text{Ar}/^{39}\text{Ar}$ muscovite dating of thrust activity:
891 a case study from the Axial Zone of the Pyrenees. *Tectonophysics*, 745, 412-429.

892 Arason, p. & Levi, S. (2010) Maximum likelihood solution for inclination-only data in paleomagnetism. *Geophysical Journal International*,
893 182, 753–771. doi:10.1111/j.1365-246X.2010.04671.x

894 Aubourg, C., & Pozzi, J. P. (2010). Toward a new < 250 C pyrrhotite–magnetite geothermometer for claystones. *Earth and Planetary*
895 *Science Letters*, 294(1-2), 47-57.

896 Aubourg, C., Pozzi, J.-P. & Kars, M. (2012) Burial, claystones remagnetization and some consequences for magnetostratigraphy.
897 *Geological Society, London, Special Publications*, 371, 181–188. doi:10.1144/SP371.4

- 898 Aubourg, C., Jackson, M., Ducoux, M., & Mansour, M. (2019). Magnetite-out and pyrrhotite-in temperatures in shales and slates. *Terra*
899 *Nova*, 31(6), 534-539.
- 900 Autran A, García-Sansegundo J (1996) Tectonique hercynienne. Carte structurale (moitié occidentale). In: Barnolas A, Chiron JC (eds)
901 Synthèse géologique at géophysique des Pyrénées, vol 1. BRGM-ITGE, Orléans-Madrid
- 902 Azor, A., Dias da Silva, Í., Gómez Barreiro, J., González-Clavijo, E., Martínez Catalán, J.R., Simancas, J.F., Martínez Poyatos, D., *et al.*
903 (2019) Deformation and Structure. in *The Geology of Iberia: A Geodynamic Approach* Regional Geology Reviews eds. Quesada, C.
904 & Oliveira, J.T., pp. 307–348, Cham: Springer International Publishing. doi:10.1007/978-3-030-10519-8_10
- 905 Barnolas, A., Gil-Peña, I., Alfageme, S., Ternet, Y., Baudin, T., & Laumonier, B. (2008). Mapa geológico de los Pirineos a escala 1:400
906 000. IGME/BRGM ISBN: 978-2- 7159-2168-9.
- 907 Beamud, E., Muñoz, J. A., Fitzgerald, P. G., Baldwin, S. L., Garcés, M., Cabrera, L., & Metcalf, J. R. (2011). Magnetostratigraphy and
908 detrital apatite fission track thermochronology in syntectonic conglomerates: constraints on the exhumation of the South-
909 Central Pyrenees. *Basin Research*, 23(3), 309-331.
- 910 Biggin, A.J., Piispa, E.J., Pesonen, L.J., Holme, R., Paterson, G.A., Veikkolainen, T. & Tauxe, L. (2015) Palaeomagnetic field intensity
911 variations suggest Mesoproterozoic inner-core nucleation. *Nature*, 526, 245–248. doi:10.1038/nature15523
- 912 Bosch, G. V., Teixell, A., Jolivet, M., Labaume, P., Stockli, D., Domènech, M., & Monié, P. (2016). Timing of Eocene–Miocene thrust
913 activity in the Western Axial Zone and Chaînons Béarnais (west-central Pyrenees) revealed by multi-method thermochronology.
914 *Comptes Rendus Geoscience*, 348(3-4), 246-256.
- 915 Casas, J.M., Álvaro, J.J., Clausen, S., Padel, M., Puddu, C., Sanz-López, J., Sánchez-García, T., *et al.* (2019) Palaeozoic Basement of the
916 Pyrenees. in *The Geology of Iberia: A Geodynamic Approach* Regional Geology Reviews eds. Quesada, C. & Oliveira, J.T., pp. 229–
917 259, Cham: Springer International Publishing. doi:10.1007/978-3-030-10519-8_8
- 918 Calvet, M., Gunnell, Y., & Laumonier, B. (2020). Denudation history and palaeogeography of the Pyrenees and their peripheral basins:
919 an 84-million-year geomorphological perspective. *Earth-Science Reviews*, 103436.
- 920 Calvín, P., Santolaria, P., Casas, A. M., & Pueyo, E. L. (2018). Detachment fold vs. ramp anticline: a gravity survey in the southern
921 Pyrenean front (External Sierras). *Geological Journal*, 53(1), 178-190.
- 922 Cámara, P., & Klimowitz, J. (1985). Interpretación geodinámica de la vertiente centro-occidental surpirenaica (Cuencas de Jaca-
923 Tresp). *Estudios geológicos*, 41(5-6), 391-404.

- 924 Casas, J. M., Domingo, F., Poblet, J., & Soler, A. (1989). On the role of the Hercynian and Alpine thrusts in the Upper Paleozoic rocks
925 of the Central and Eastern Pyrenees. *Geodinamica Acta*, 3(2), 135-147.
- 926 Casas, A. M., Oliva, B., Román-Berdiel, T., & Pueyo, E. (2003). Basement deformation: tertiary folding and fracturing of the Variscan
927 Bielsa granite (Axial zone, central Pyrenees). *Geodinamica acta*, 16(2-6), 99-117.
- 928 Choukroune, P., & Séguret, M. (1973). Carte structurale des Pyrénées, 1/500.000, Université de Montpellier – ELF Aquitaine
- 929 Crognier, N., Hoareau, G., Aubourg, C., Dubois, M., Lacroix, B., Branellec, M., ... & Vennemann, T. (2018). Syn-orogenic fluid flow in
930 the Jaca basin (south Pyrenean fold and thrust belt) from fracture and vein analyses. *Basin Research*, 30(2), 187-216.
- 931 Crouzet, C., Stang, H., Appel, E., Schill, E., & Gautam, P. (2001). Detailed analysis of successive pTRMs carried by pyrrhotite in
932 Himalayan metacarbonates: an example from Hidden Valley, Central Nepal. *Geophysical Journal International*, 146(3), 607-
933 618.
- 934 Deenen, M.H.L., Langereis, C.G., Hinsbergen, D.J.J. van & Biggin, A.J. (2011) Geomagnetic secular variation and the statistics of
935 palaeomagnetic directions. *Geophysical Journal International*, **186**, 509–520. doi:10.1111/j.1365-246X.2011.05050.x
- 936 Debon and Guitard (1996) Métamorphisme at plutonisme hercyniens. Carte de synthèse. In: Barnolas A, Chiron, JC (eds) Synthèse
937 géologique et géophysique des Pyrénées, vol 1. BRGM-ITGE, Orle'ans-Madrid
- 938 Dekkers, M. J. (1989) Magnetic properties of natural pyrrhotite. II. High- and low-temperature behaviour of Jrs and TRM as function
939 of grain size. *Physics of the Earth and Planetary Interiors*, **57**, 266–283. doi:10.1016/0031-9201(89)90116-7
- 940 Dekkers, Mark J. (2012) End-member modelling as an aid to diagnose remagnetization: a brief review. *Geological Society, London, Special
941 Publications*, **371**, 253–269. doi:10.1144/SP371.12
- 942 Denèle Y, Paquette JL, Olivier Ph, Barbey P (2011) Permian granites in the Pyrenees: the Aya pluton (Basque Country). *Terra Nova*
943 00:1–9
- 944 Denèle, Y., Laumonier, B., Paquette, J. L., Olivier, P., Gleizes, G., & Barbey, P. (2014). Timing of granite emplacement, crustal flow
945 and gneiss dome formation in the Variscan segment of the Pyrenees. *Geological Society, London, Special Publications*, 405(1), 265-
946 287.
- 947 Dias da Silva, Í., González Clavijo, E. & Díez-Montes, A. (2020) The collapse of the Variscan belt: a Variscan lateral extrusion thin-
948 skinned structure in NW Iberia. *International Geology Review*, **00**, 1–37, Taylor & Francis. doi:10.1080/00206814.2020.1719544

- 949 Dinarès-Turell, J. (1994). Remagnetizations associated to diagenesis and their relationship with thrust sheet emplacement in the Southern
950 Pyrenees. *Geocaceta*, 15, 105-108.
- 951 Dinares-Turell, J., & Garcia-Senz, J. (2000). Remagnetization of Lower Cretaceous limestones from the southern Pyrenees and relation
952 to the Iberian Plate geodynamic evolution. *Journal of Geophysical Research*, 105(B8), 19-19,418. doi:10.1029/2000JB900136.
- 953 Dinarès, J., McClelland, E., & Santanach, P. (1992). Contrasting rotations within thrust sheets and kinematics of thrust tectonics as
954 derived from palaeomagnetic data: an example from the Southern Pyrenees. In *Thrust tectonics* (pp. 265-275). Springer,
955 Dordrecht.
- 956 Domeier, M. (2016) A plate tectonic scenario for the Iapetus and Rheic Oceans. *Gondwana Research*, 36, 275–295, Elsevier.
- 957 Domeier, M. & Torsvik, T.H. (2014) Plate tectonics in the late Paleozoic. *Geoscience Frontiers*, 5, 303–350, Elsevier Ltd.
958 doi:10.1016/j.gsf.2014.01.002
- 959 Domeier, M. & Torsvik, T.H. (2019) Full-plate modelling in pre-Jurassic time. *Geological Magazine*, 156, 261–280, Cambridge University
960 Press. doi:10.1017/S0016756817001005
- 961 Edel, J.B., Schulmann, K., Lexa, O. & Lardeaux, J.M. (2018) Late Palaeozoic palaeomagnetic and tectonic constraints for amalgamation
962 of Pangea supercontinent in the European Variscan belt. *Earth-Science Reviews*, 177, 589–612, Elsevier.
963 doi:10.1016/j.earscirev.2017.12.007
- 964 Egl, R. (2004) Characterization of individual rock magnetic components by analysis of remanence curves. *Physics and Chemistry of the
965 Earth*, 29, 851–867. doi:10.1016/j.pce.2004.04.001
- 966 Enkin, R. J., & Watson, G. S. (1996). Statistical analysis of palaeomagnetic inclination data. *Geophysical Journal International*, 126(2),
967 495-504
- 968 Fernández-Lozano, J., Pastor-Galán, D., Gutiérrez-Alonso, G. & Franco, P. (2016) New kinematic constraints on the Cantabrian
969 orocline: A paleomagnetic study from the Peñalba and Truchas synclines, NW Spain. *Tectonophysics*, 681, 195–208, Elsevier B.V.
970 doi:10.1016/j.tecto.2016.02.019
- 971 Fernández-Suárez, J., Gutiérrez-Alonso, G., Pastor-Galán, D., Hofmann, M., Murphy, J.B. & Linnemann, U. (2014) The Ediacaran-
972 Early Cambrian detrital zircon record of NW Iberia: Possible sources and paleogeographic constraints. *International Journal of
973 Earth Sciences*, 103, 1335–1357. doi:10.1007/s00531-013-0923-3

- 974 Fillon, C., & van der Beek, P. (2012). Post-orogenic evolution of the southern Pyrenees: Constraints from inverse thermo-kinematic
975 modelling of low-temperature thermochronology data. *Basin Research*, 24(4), 418-436.
- 976 Fisher, R. (1953) Dispersion on a Sphere. *Proceedings of the Royal Society A: Mathematical, Physical and Engineering Sciences*, 217, 295–305.
977 doi:10.1098/rspa.1953.0064
- 978 Fitzgerald, P. G., Muñoz, J. A., Coney, P. J., & Baldwin, S. L. (1999). Asymmetric exhumation across the Pyrenean orogen: implications
979 for the tectonic evolution of a collisional orogen. *Earth and Planetary Science Letters*, 173(3), 157-170.
- 980 Franke, W., Cocks, L.R.M. & Torsvik, T.H. (2017) The Palaeozoic Variscan oceans revisited. *Gondwana Research*, 48, 257–284.
981 doi:10.1016/j.gr.2017.03.005
- 982 Fuller, M. D. (1963). Magnetic anisotropy and paleomagnetism. *Journal of Geophysical Research*, 68(1), 293-309.
- 983 Garcés, M., López-Blanco, M., Valero, L., Beamud, E., Muñoz, J. A., Oliva-Urcia, B., ... & Cabrera, L. (2020). Paleogeographic and
984 sedimentary evolution of the South Pyrenean foreland basin. *Marine and Petroleum Geology*, 113, 104105.
- 985 García-Sansegundo, J., Poblet, J., Alonso, J.L. & Clariana, P. (2011) Hinterland-foreland zonation of the Variscan orogen in the Central
986 Pyrenees: comparison with the northern part of the Iberian Variscan Massif. *Geological Society, London, Special Publications*, 349,
987 169–184, Geological Society of London. doi:10.1144/SP349.9
- 988 GEODE, 2011. Mapa Geológico Digital continuo de España [on-line]. In: Navas, J. (Ed.), Sistema de Información Geológica Continua:
989 SIGECO. IGME.
- 990 Gil-Peña, I., Oliva, B., Pueyo, E. L., Barnolas, A., 2005. Datos preliminares de la remagnetización Estefaniense del Ordovícico
991 Superior del Pirineo Centro-meridional, implicaciones estructurales. *Ordovícico Catalán. MAGIBER-IV* (Vigo), 47- 50.
- 992 Gil-Peña, I.; Oliva, B.; Pueyo, E. L.; Barnolas, A. Remagnetización Stefaniense-Pérmica del Ordovícico de la Zona Axial meridional del
993 Pirineo Central; implicaciones paleogeográficas y tectónicas posthercínicas. *Proceedings MAGIBER IV- IV Paleomagnetismo*
994 *en España y Portugal* (Vigo), 47-50 (2006)
- 995 Gleizes, G., Leblanc, D., & Bouchez, J. L. (1997). Variscan granites of the Pyrenees revisited: their role as syntectonic markers of the
996 orogen. *Terra Nova*, 9(1), 38-41.

- 997 Gleizes, G., Leblanc, D., Santana, V., Olivier, P., & Bouchez, J. L. (1998). Sigmoidal structures featuring dextral shear during
998 emplacement of the Hercynian granite complex of Cauterets–Panticosa (Pyrenees). *Journal of Structural Geology*, 20(9-10),
999 1229-1245.
- 1000 Gong, Z., Dekkers, M.J., Heslop, D. & Mullender, T.A.T.T. (2009) End-member modelling of isothermal remanent magnetization
1001 (IRM) acquisition curves: a novel approach to diagnose remagnetization. *Geophysical Journal International*, **178**, 693–701.
1002 doi:10.1111/j.1365-246X.2009.04220.x
- 1003 Gong, Z., Langereis, C.G. & Mullender, T.A.T. (2008) The rotation of Iberia during the Aptian and the opening of the Bay of Biscay.
1004 *Earth and Planetary Science Letters*, **273**, 80–93.
- 1005 Gutiérrez-Alonso, Gabriel, Collins, A.S., Fernández-Suárez, J., Pastor-Galán, D., González-Clavijo, E., Jourdan, F., Weil, A.B., *et al.*
1006 (2015) Dating of lithospheric buckling: $^{40}\text{Ar}/^{39}\text{Ar}$ ages of syn-orocline strike-slip shear zones in northwestern Iberia.
1007 *Tectonophysics*, **643**, 44–54, Elsevier B.V. doi:10.1016/j.tecto.2014.12.009
- 1008 Gutiérrez-Alonso, G., López-Carmona, A., Núñez-Guerrero, E., García, A.M., Fernández-Suárez, J., Pastor-Galán, D., Gutiérrez-
1009 Marco, J.C., *et al.* (2020) Neoproterozoic-Palaeozoic detrital sources in the Variscan foreland of northern Iberia: primary vs.
1010 recycled sediments. *Geological Society, London, Special Publications*, **503**, Geological Society of London. doi:10.1144/SP503-2020-21
- 1011 Heslop, D., Dekkers, M.J., Kruiver, P.P. & Van Oorschot, I.H.M. (2002) Analysis of isothermal remanent magnetization acquisition
1012 curves using the expectation-maximization algorithm. *Geophysical Journal International*, **148**, 58–64. doi:10.1046/j.0956-
1013 540x.2001.01558.x
- 1014 Heslop, D. & Dillon, M. (2007) Unmixing magnetic remanence curves without a priori knowledge. *Geophysical Journal International*, **170**,
1015 556–566, Oxford University Press. doi:10.1111/j.1365-246X.2007.03432.x
- 1016 Heslop, D., McIntosh, G. & Dekkers, M.J. (2004) Using time- and temperature-dependent Preisach models to investigate the limitations
1017 of modelling isothermal remanent magnetization acquisition curves with cumulative log Gaussian functions. *Geophysical Journal*
1018 *International*, **157**, 55–63, Oxford University Press. doi:10.1111/j.1365-246X.2004.02155.x
- 1019 Hoareau, G., Crognier, N., Lacroix, B., Aubourg, C., Roberts, N. M., Niemi, N., ... & Ruiz, I. S. (2021). Combination of $\Delta 47$ and U-Pb
1020 dating in tectonic calcite veins unravel the last pulses related to the Pyrenean Shortening (Spain). *Earth and Planetary Science*
1021 *Letters*, 553, 116636.

- 1022 Huang, W., Dupont-Nivet, G., Lippert, P.C., Hinsbergen, D.J.J. van, Dekkers, M.J., Guo, Z., Waldrip, R., *et al.* (2015) Can a primary
1023 remanence be retrieved from partially remagnetized Eocene volcanic rocks in the Nanmulin Basin (southern Tibet) to date the
1024 India-Asia collision? *Journal of Geophysical Research: Solid Earth*, **120**, 42–66. doi:10.1002/2014JB011599
- 1025 Huang, W., Lippert, P.C., Zhang, Y., Jackson, M.J., Dekkers, M.J., Li, J., Hu, X., *et al.* (2017) Remagnetization of carbonate rocks in
1026 southern Tibet: Perspectives from rock magnetic and petrographic investigations. *Journal of Geophysical Research: Solid Earth*, **122**,
1027 2434–2456. doi:10.1002/2017JB013987
- 1028 Huyghe, D., Mouthereau, F., Castellort, S., Filleaudeau, P. Y., & Emmanuel, L. (2009). Paleogene propagation of the southern Pyrenean
1029 thrust wedge revealed by finite strain analysis in frontal thrust sheets: Implications for mountain building. *Earth and Planetary
1030 Science Letters*, 288(3-4), 421-433.
- 1031 Izquierdo-Llavall, E., Aldega, L., Cantarelli, V., Corrado, S., Gil-Peña, I., Invernizzi, C., & Casas, A. M. (2013). On the origin of cleavage
1032 in the Central Pyrenees: structural and paleo-thermal study. *Tectonophysics*, 608, 303-318.
- 1033 Izquierdo-Llavall, E., Casas-Sainz, A., Oliva-Urcia, B., & Scholger, R. (2014). Palaeomagnetism and magnetic fabrics of the Late
1034 Palaeozoic volcanism in the Castejón-Laspaúles basin (Central Pyrenees). Implications for palaeoflow directions and basin
1035 configuration. *Geological Magazine*, 151(5), 777-797.
- 1036 Izquierdo-Llavall, E., Sainz, A. C., Oliva-Urcia, B., Burmester, R., Pueyo, E. L., & Housen, B. (2015). Multi-episodic remagnetization
1037 related to deformation in the Pyrenean Internal Sierras. *Geophysical Journal International*, 201(2), 891-914.
- 1038 Izquierdo-Llavall, E., Casas-Sainz, A. M., Oliva-Urcia, B., Villalaín, J. J., Pueyo, E., & Scholger, R. (2018). Rotational kinematics of
1039 basement antiformal stacks: Paleomagnetic study of the western Noguera Zone (Central Pyrenees). *Tectonics*, 37(10), 3456-3478.
- 1040 Izquierdo-Llavall, E., Menant, A., Aubourg, C., Callot, J. P., Hoareau, G., Camps, P., ... & Lahfid, A. (2020) Pre-orogenic folds and syn-
1041 orogenic basement tilts in an inverted hyperextended margin: the northern Pyrenees case study. *Tectonics*, e2019TC005719.
- 1042 Jackson, M., Rochette, P., Fillion, G., Banerjee, S. & Marvin, J. (1993) Rock magnetism of remagnetized Paleozoic carbonates: Low-
1043 temperature behavior and susceptibility characteristics. *Journal of Geophysical Research: Solid Earth*, **98**, 6217–6225.
1044 doi:https://doi.org/10.1029/92JB01319
- 1045 Jolivet, M., Labaume, P., Monié, P., Brunel, M., Arnaud, N., & Campani, M. (2007). Thermochronology constraints for the propagation
1046 sequence of the south Pyrenean basement thrust system (France-Spain). *Tectonics*, 26(5).

- 1047 Juárez, M. T., Lowrie, W., Osete, M. L., & Meléndez, G. (1998). Evidence of widespread Cretaceous remagnetisation in the Iberian
1048 Range and its relation with the rotation of Iberia. *Earth and Planetary Science Letters*, 160(3-4), 729-743.
- 1049 Kirschvink, J.L. (1980) The least-squares line and plane and the analysis of palaeomagnetic data. *Geophysical Journal International*, 62, 699–
1050 718. doi:10.1111/j.1365-246X.1980.tb02601.x
- 1051 Kleinsmiede, W.F.J. (1960) Geology of the Valle de Arán (Central Pyrenees). *Leidse Geologische Mededelingen*, 25, 129–245.
- 1052 Koymans, M.R., Hinsbergen, D.J.J. van, Pastor-Galán, D., Vaes, B. & Langereis, C.G. (2020) Towards FAIR Paleomagnetic Data
1053 Management Through Paleomagnetism.org 2.0. *Geochemistry, Geophysics, Geosystems*, 21, e2019GC008838.
1054 doi:10.1029/2019GC008838
- 1055 Koymans, M.R.R., Langereis, C.G.G., Pastor-Galán, D. & Hinsbergen, D.J.J.J.D.J.J. van. (2016) Paleomagnetism.org: An online multi-
1056 platform open source environment for paleomagnetic data analysis. *Computers and Geosciences*, 93, 127–137, Elsevier.
1057 doi:10.1016/j.cageo.2016.05.007
- 1058 Kruiver, P.P., Dekkers, M.J. & Heslop, D. (2001) Quantification of magnetic coercivity components by the analysis of acquisition curves
1059 of isothermal remanent magnetisation. *Earth and Planetary Science Letters*, 189, 269–276. doi:10.1016/S0012-821X(01)00367-3
- 1060 Kuiper, K.F., Deino, A., Hilgen, F.J., Krijgsman, W., Renne, P.R. & Wijbrans, J.R. (2008) Synchronizing Rock Clocks of Earth History.
1061 *Science*, 320, 500–504, American Association for the Advancement of Science. doi:10.1126/science.1154339
- 1062 Keller, P., Lowrie, W., & Gehring, A. U. (1994). Palaeomagnetic evidence for post-thrusting tectonic rotation in the Southeast Pyrenees,
1063 Spain. *Tectonophysics*, 239(1-4), 29-42.
- 1064 Labaume, P., Séguret, M., & Seyve, C. (1985). Evolution of a turbiditic foreland basin and analogy with an accretionary prism: Example
1065 of the Eocene south-Pyrenean basin. *Tectonics*, 4(7), 661-685.
- 1066 Labaume, P., & Teixell, A. (2018). 3D structure of subsurface thrusts in the eastern Jaca Basin, southern Pyrenees. *Geologica Acta*, 16(4),
1067 477-498.
- 1068 Lagabrielle, Y., Labaume, P. and de Saint Blanquat, M., 2010. Mantle exhumation, crustal denudation, and gravity tectonics during
1069 Cretaceous rifting in the Pyrenean realm (SW Europe): Insights from the geological setting of the lherzolite bodies. *Tectonics*,
1070 29(4).

- 1071 Lanaja, J. M., 1987. Contribución de la exploración petrolífera al conocimiento de la Geología de España.
1072 <http://info.igme.es/geologiasubsuelo/GeologiaSubsuelo/Documents.aspx>. Instituto Geológico y Minero de España Ed., .465
1073 pp., 17 mapas.
- 1074 Leite Mendes, B.D., Pastor-Galán, D., Dekkers, M.J. & Krijgsman, W. (2021) Avalonia, get bent! – Paleomagnetism from SW Iberia
1075 confirms the Greater Cantabrian Orocline. *Geoscience Frontiers*, **12**, 805–825. doi:10.1016/j.gsf.2020.07.013
- 1076 Martínez-Peña, M., & Casas-Sainz, A. (2003). Cretaceous–tertiary tectonic inversion of the Cotiella Basin (southern Pyrenees, Spain).
1077 *International Journal of Earth Sciences*, 92(1), 99-113.
- 1078 Maxbauer, D.P., Feinberg, J.M., Fox, D.L. (2016). MAX UnMix: A web application for unmixing magnetic coercivity distributions.
1079 *Comp. Geosci.*, 95, 140-145. doi:10.1016/j.cageo.2016.07.009
- 1080 McCabe, C., Van der Voo, R., Peacor, D. R., Scotese, C. R., & Freeman, R. (1983). Diagenetic magnetite carries ancient yet secondary
1081 remanence in some Paleozoic sedimentary carbonates. *Geology*, 11(4), 221-223.
- 1082 McCabe, C., & Elmore, R. D. (1989). The occurrence and origin of late Paleozoic remagnetization in the sedimentary rocks of North
1083 America. *Reviews of Geophysics*, 27(4), 471-494.
- 1084 McClelland, E. A., & McCaig, A. M. (1988). Palaeomagnetic estimates of total rotation in basement thrust sheets, Axial Zone, Southern
1085 Pyrenees. *Cuadernos de Geología Ibérica*, 12, 181-193.
- 1086 McClelland, E., & McCaig, A. M. (1989). Palaeomagnetic estimates of rotations in compressional regimes and potential discrimination
1087 between thin-skinned and deep crustal deformation. In: *Paleomagnetic rotations and continental deformation* (Eds: Kissel, C.;
1088 Laj, C.) NATO ASI Series C, 254, 365-379. Springer, Dordrecht.
- 1089 McFadden, P.L.L. & McElhinny, M.W. (1988) The combined analysis of remagnetization circles and direct observations in
1090 palaeomagnetism. *Earth and Planetary Science Letters*, **87**, 161–172. doi:10.1016/0012-821X(88)90072-6
- 1091 Millán-Garrido, H.; Oliva-Urcia, B., & Pocoví-Juan, A. (2006). La transversal de Gavarnie-Guara; estructura y edad de los mantos de
1092 Gavarnie, Guara-Gedre y Guarga (Pirineo centro-occidental). *Geogaceta*, 40, 35-38.
- 1093 Mochales, T., Casas, A. M., Pueyo, E. L., & Barnolas, A. (2012). Rotational velocity for oblique structures (Boltaña anticline, Southern
1094 Pyrenees). *Journal of Structural Geology*, 35, 2-16.

- 1095 Mochales, T., Pueyo, E. L., Casas, A. M., & Barnolas, A. (2016). Restoring paleomagnetic data in complex superposed folding settings:
1096 the Boltaña anticline (Southern Pyrenees). *Tectonophysics*, 671, 281-298.
- 1097 Mujal, E., Fortuny, J., Pérez-Cano, J., Dinarès-Turell, J., Ibáñez-Insa, J., Oms, O., . . . Anadón, P. (2017). Integrated multi-stratigraphic
1098 study of the Coll de Terrers late Permian–Early Triassic continental succession from the Catalan Pyrenees (NE Iberian
1099 Peninsula): A geologic reference record for equatorial Pangaea. *Global and Planetary Change*, 159, 46-60.
1100 doi:<https://doi.org/10.1016/j.gloplacha.2017.10.004>
- 1101 Mullender, T. A. T., Frederichs, C., Hilgenfeldt, L. V. de Groot, K. Fabian, and M. J. Dekkers (2016). Automated paleomagnetic and
1102 rock magnetic data acquisition with an in-line horizontal “2G” system. *Geochem. Geophys. Geosyst.*, 17, 3546–3559.
1103 doi:10.1002/2016GC006436.
- 1104 Müller, R.D., Zahirovic, S., Williams, S.E., Cannon, J., Seton, M., Bower, D.J., Tetley, M.G., *et al.* (2019) A Global Plate Model Including
1105 Lithospheric Deformation Along Major Rifts and Orogens Since the Triassic. *Tectonics*, 38, 1884–1907, Blackwell Publishing
1106 Ltd. doi:10.1029/2018TC005462
- 1107 Muñoz, J. A., Beamud, E., Fernández, O., Arbués, P., Dinarès-Turell, J., & Poblet, J. (2013). The Ainsa Fold and thrust oblique zone of
1108 the central Pyrenees: Kinematics of a curved contractional system from paleomagnetic and structural data. *Tectonics*, 32(5), 1142-
1109 1175.
- 1110 Muñoz, J. A. (1992). Evolution of a continental collision belt: ECORS-Pyrenees crustal balanced cross-section. In *Thrust tectonics* (pp.
1111 235-246). Springer, Dordrecht.
- 1112 Muñoz, J. A., Mencos, J., Roca, E., Carrera, N., Gratacós, O., Ferrer, O., & Fernández, Ò. (2018). The structure of the South-Central-
1113 Pyrenean fold and thrust belt as constrained by subsurface data. *Geologica Acta*, 16(4), 439-460.
- 1114 Muñoz, J. A. (2019). Alpine Orogeny: Deformation and Structure in the Northern Iberian Margin (Pyrenees sl). In *The Geology of Iberia:
1115 A Geodynamic Approach* (pp. 433-451). Springer, Cham.
- 1116 Muñoz, J. A., Martínez, A., & Vergés, J. (1986). Thrust sequences in the eastern Spanish Pyrenees. *Journal of Structural Geology*, 8(3-
1117 4), 399-405.
- 1118 Nance, R.D., Gutiérrez-Alonso, G., Keppie, J.D., Linnemann, U., Murphy, J.B., Quesada, C., Strachan, R.A., *et al.* (2010) Evolution of
1119 the Rheic Ocean. *Gondwana Research*, 17, 194–222. doi:10.1016/j.gr.2009.08.001

- 1120 Neres, M., Miranda, J.M. & Font, E. (2013) Testing Iberian kinematics at Jurassic-Cretaceous times. *Tectonics*, **32**, 1312–1319.
1121 doi:10.1002/tect.20074
- 1122 Nirrengarten, M., Manatschal, G., Tugend, J., Kuszniir, N., & Sauter, D. (2018). Kinematic evolution of the southern North Atlantic:
1123 Implications for the formation of hyperextended rift systems. *Tectonics*, *37*(1), 89-118.
- 1124 Oliva-Urcia, B., & Pueyo, E. L. (2007a). Gradient of shortening and vertical-axis rotations in the Southern Pyrenees (Spain), insights
1125 from a synthesis of paleomagnetic data. *Revista de la Sociedad Geológica de España*, *20*(1-2), 105-118.
- 1126 Oliva-Urcia, B., & Pueyo, E. L. (2007b). Rotational basement kinematics deduced from remagnetized cover rocks (Internal Sierras,
1127 southwestern Pyrenees). *Tectonics*, *26*(4).
- 1128 Oliva-Urcia, B., & Pueyo, E. L. (2019). Paleomagnetism in structural geology and tectonics. In *Teaching methodologies in structural geology and*
1129 *tectonics* (pp. 55-121). Springer, Singapore.
- 1130 Oliva-Urcia, B., Pueyo, E. L., & Larrasoña, J. C. (2008). Magnetic reorientation induced by pressure solution: a potential mechanism
1131 for orogenic-scale remagnetizations. *Earth and Planetary Science Letters*, *265*(3-4), 525-534.
- 1132 Oliva-Urcia, B., Casas, A. M., Pueyo, E. L., Román-Berdiel, T., & Geissman, J. W. (2010). Paleomagnetic evidence for dextral strike-slip
1133 motion in the Pyrenees during alpine convergence (Mauléon basin, France). *Tectonophysics*, *494*(3-4), 165-179.
- 1134 Oliva-Urcia, B., Pueyo, E. L., Larrasoña, J. C., Casas, A. M., Román-Berdiel, T., Van der Voo, R., & Scholger, R. (2012). New and
1135 revisited paleomagnetic data from Permian–Triassic red beds: Two kinematic domains in the west-central
1136 Pyrenees. *Tectonophysics*, *522*, 158-175.
- 1137 Oliveira, J.T., Quesada, C., Pereira, Z., Matos, J.X., Solá, A.R., Rosa, D., Albardeiro, L., *et al.* (2019) South Portuguese Terrane: A
1138 Continental Affinity Exotic Unit. in *The Geology of Iberia: A Geodynamic Approach* Regional Geology Reviews eds. Quesada, C. &
1139 Oliveira, J.T., pp. 173–206, Cham: Springer International Publishing. doi:10.1007/978-3-030-10519-8_6
- 1140 Parés, J.M., 2015. Sixty years of anisotropy of magnetic susceptibility in deformed sedimentary rocks. *Frontiers in Earth Science*, *3*, p.4.
- 1141 Pastor-Galan, D., Groenewegen, T., Brouwer, D., Krijgsman, W. & Dekkers, M.J. (2015) One or two oroclines in the Variscan orogen
1142 of Iberia? Implications for Pangea amalgamation. *Geology*, **43**, 527–530. doi:10.1130/G36701.1
- 1143 Pastor-Galán, Daniel, Nance, R.D., Murphy, J.B. & Spencer, C.J. (2019) Supercontinents: myths, mysteries, and milestones. *Geological*
1144 *Society, London, Special Publications*, **470**, 39–64, Geological Society of London. doi:10.1144/SP470.16

- 1145 Pastor-Galán, D, Ursem, B., Meere, P.A. & Langereis, C. (2015) Extending the Cantabrian Orocline to two continents (from Gondwana
1146 to Laurussia). Paleomagnetism from South Ireland. *Earth and Planetary Science Letters*, **432**. doi:10.1016/j.epsl.2015.10.019
- 1147 Pastor-Galán, Daniel, Dekkers, M.J.M.J., Gutiérrez-Alonso, G., Brouwer, D., Groenewegen, T., Krijgsman, W., Fernández-Lozano,
1148 J., *et al.* (2016) Paleomagnetism of the Central Iberian curve's putative hinge: Too many oroclines in the Iberian Variscides.
1149 *Gondwana Research*, **39**, 96–113, International Association for Gondwana Research. doi:10.1016/j.gr.2016.06.016
- 1150 Pastor-Galán, Daniel, Gutiérrez-Alonso, G., Dekkers, M.J.M.J. & Langereis, C.G.C.G.C.G. (2017) Paleomagnetism in Extremadura
1151 (Central Iberian zone, Spain) Paleozoic rocks: extensive remagnetizations and further constraints on the extent of the Cantabrian
1152 orocline. *Journal of Iberian Geology*, **43**, 583–600, Springer International Publishing. doi:10.1007/s41513-017-0039-x
- 1153 Pastor-Galán, Daniel, Gutiérrez-Alonso, G., Murphy, J.B.B., Fernández-Suárez, J., Hofmann, M. & Linnemann, U. (2013) Provenance
1154 analysis of the Paleozoic sequences of the northern Gondwana margin in NW Iberia: Passive margin to Variscan collision and
1155 orocline development. *Gondwana Research*, **23**, 1089–1103, International Association for Gondwana Research.
1156 doi:10.1016/j.gr.2012.06.015
- 1157 Pastor-Galán, Daniel, Gutiérrez-Alonso, G. & Weil, A.B. (2011) Orocline timing through joint analysis: Insights from the Ibero-
1158 Armorican Arc. *Tectonophysics*, **507**, 31–46. doi:10.1016/j.tecto.2011.05.005
- 1159 Pastor-Galán, Daniel, Gutiérrez-Alonso, G. & Weil, A.B. (2020) The enigmatic curvature of Central Iberia and its puzzling kinematics.
1160 *Solid Earth*, **11**, 1247–1273, Copernicus GmbH. doi:https://doi.org/10.5194/se-11-1247-2020
- 1161 Pastor-Galán, Daniel, Pueyo, E.L., Diederer, M., García-Lasanta, C. & Langereis, C.G. (2018) Late Paleozoic Iberian Orocline(s) and
1162 the Missing Shortening in the Core of Pangea. Paleomagnetism From the Iberian Range. *Tectonics*, **37**, 3877–3892, John Wiley
1163 & Sons, Ltd. doi:10.1029/2018TC004978
- 1164 Pereira, M.F., Castro, A., Chichorro, M., Fernández, C., Díaz-Alvarado, J., Martí, J. & Rodríguez, C. (2014) Chronological link between
1165 deep-seated processes in magma chambers and eruptions: Permo-Carboniferous magmatism in the core of Pangaea (Southern
1166 Pyrenees). *Gondwana Research*, **25**, 290–308, Elsevier. doi:10.1016/J.GR.2013.03.009
- 1167 Pérez-Cáceres, I., Martínez Poyatos, D., Simancas, J.F. & Azor, A. (2017) Testing the Avalonian affinity of the South Portuguese Zone
1168 and the Neoproterozoic evolution of SW Iberia through detrital zircon populations. *Gondwana Research*, **42**, 177–192.
1169 doi:10.1016/j.gr.2016.10.010
- 1170 Porquet, M., Pueyo, E. L., Román-Berdiel, T., Olivier, P., Longares, L. A., Cuevas, J., ... & Auréjac, J. B. (2017). Anisotropy of magnetic
1171 susceptibility of the Pyrenean granites. *Journal of Maps*, **13**(2), 438-448.

- 1172 Pueyo, E. L. (2000). Rotaciones paleomagnéticas en sistemas de pliegues y cabalgamientos. Tipos, causas, significado y aplicaciones
1173 (ejemplos del Pirineo Aragonés). *Unpublished PhD thesis, Universidad de Zaragoza, 296.*
- 1174 Pueyo, E. L., Sussman, A. J., Oliva-Urcia, B., & Cifelli, F. (2016a). Palaeomagnetism in fold and thrust belts: use with caution. *Geological
1175 Society, London, Special Publications, 425(1)*, 259-276.
- 1176 Pueyo, E. L., Beamud, E., Muñoz, J. A., Rodríguez-Pintó, A., & San Miguel, G. (2016b). Remagnetización alpina en la Serra del Cadí
1177 (Pirineo Oriental). *Geo-Temas, 16 (1)* 869-872.
- 1178 Pueyo, E. L., García-Lasanta, C., López, M. A., Oliván, C., San Miguel, G., Gil-Garbi, H et al. the GeoKin3DPyr working group (2017).
1179 Metodología para el desarrollo de la BBDD paleomagnética de Iberia (EPOS-DDSS Iberian Paleomagnetism). In MAGIBER X.
1180 (pp. 94–99). Instituto de Investigación en Ciencias Ambientales (IUCA). Universidad de Zaragoza. ISBN: 978-84-16723-40-9
- 1181 Pueyo, E. L., Oliva-Urcia, B., Sánchez-Moreno, E.M., Arenas, C., Silva-Casal, R., Calvín, P., Santolaria, P., García-Lasanta, C., Oliván,
1182 C., Gil-Imaz, A., Compaired, F., Casas, A.M., Pocoví, A. (2021a). The geometry and kinematics of the Southwestern termination
1183 of the Pyrenees; A field guide to the Santo Domingo anticline. In *Structural Geology and Tectonics Field Guidebook -*
1184 *Mukherjee, S. (Editor). Chapter 3, 52pp. Springer. ISBN 978-3-030-60142-3*
- 1185 Pueyo, E.L.; Rodríguez-Pintó, A.; Serra-Kiel, J.; Barnolas, A. (2021b in press). The chronology and rotational kinematics in the Eastern
1186 Jaca Basin (Southern Pyrenees): Las Bellostas section. *Geologica Acta.*
- 1187 Puigdefàbregas, C., Muñoz, J. A., & Vergés, J. (1992). Thrusting and foreland basin evolution in the southern Pyrenees. In *Thrust
1188 tectonics (pp. 247-254). Springer, Dordrecht.*
- 1189 Robador, A., Samsó, J.M., Ramajo, J., Barnolas, A., Clariana, P., Martín, S. Gil, I (2019) (2; Mapa Geológico Digital continuo E. 1:50.000,
1190 Zona Pirineos Vasco-Cantábrica (Zona-1600). in GEODE. Mapa Geológico Digital continuo de España.
1191 <http://info.igme.es/cartografiadigital/geologica/geodezona.aspx?id=Z1600>
- 1192 Ramón, M. J., Pueyo, E. L., Oliva-Urcia, B., Scholger, R., Román-Berdiel, M. T., & Casas, A. M. (2016). Squeezing paleomagnetic
1193 information using virtual directions; an example from the Bielsa granite (Axial Pyrenees). *Geotemas, 16(1)*, 873-876.
- 1194 Ramón, M. J., Pueyo, E. L., Oliva-Urcia, B., & Larrasoana, J. C. (2017). Virtual directions in paleomagnetism: A global and rapid
1195 approach to evaluate the NRM components. *Frontiers in Earth Science, 5*, 8.

- 1196 Ribeiro, M.L., Reche, J., López-Carmona, A., Aguilar, C., Bento dos Santos, T., Chichorro, M., Dias da Silva, Í., *et al.* (2019) Variscan
1197 Metamorphism. in *The Geology of Iberia: A Geodynamic Approach* Regional Geology Reviews eds. Quesada, C. & Oliveira, J.T., pp.
1198 431–495, Cham: Springer International Publishing. doi:10.1007/978-3-030-10519-8_12
- 1199 Robardet, M. (2003) The Armorica ‘microplate’: fact or fiction? Critical review of the concept and contradictory palaeobiogeographical
1200 data. *Palaeogeography, Palaeoclimatology, Palaeoecology*, **195**, 125–148. doi:10.1016/S0031-0182(03)00305-5
- 1201 Rodríguez-Pintó, A., Pueyo, E. L., Calvín, P., Sánchez, E., Ramajo, J., Casas, A. M., ... & Román, T. (2016). Rotational kinematics of a
1202 curved fold: The Balzes anticline (Southern Pyrenees). *Tectonophysics*, *677*, 171-189.
- 1203 Rouvier, H., Henry, B., & Le Goff, M. (2012). Mise en évidence par le paléomagnétisme de rotations régionales dans la virgation des
1204 Corbières (France). *Bulletin de la Société géologique de France*, *183*(5), 409-424.
- 1205 Santolaria, P., Ayala, C., Pueyo, E. L., Rubio, F. M., Soto, R., Calvín, P., ... & Casas-Sainz, A. M. (2020). Structural and geophysical
1206 characterization of the western termination of the South Pyrenean triangle zone. *Tectonics*, *39*(8), e2019TC005891.
- 1207 Scheepers, P. J. J., & Zijdeveld, J. D. A. (1992). Stacking in Paleomagnetism: application to marine sediments with weak
1208 NRM. *Geophysical Research Letters*, *19*(14), 1519-1522.
- 1209 Schmidt, P. W. (1982). Linearity spectrum analysis of multi-component magnetizations and its application to some igneous rocks from
1210 south-eastern Australia. *Geophysical Journal International*, *70*(3), 647-665.
- 1211 Schwarz, E. J. (1963). A paleomagnetic investigation of Permo-Triassic red beds and andesites from the Spanish Pyrenees. *Journal of*
1212 *Geophysical Research*, *68*(10), 3265-3271.
- 1213 Schwarz, E.J. (1974) Magnetic Fabric in Massive Sulfide Deposits. *Canadian Journal of Earth Sciences*, **11**, 1669–1675, NRC Research Press
1214 Ottawa, Canada. doi:10.1139/e74-165
- 1215 Schwarz, E.J. & Vaughan, D.J. (1972) Magnetic Phase Relations of Pyrrhotite. *Journal of geomagnetism and geoelectricity*, **24**, 441–458.
1216 doi:10.5636/jgg.24.441
- 1217 Shaw, J., Johnston, S.T. & Gutiérrez-Alonso, G. (2015) Orocline formation at the core of Pangea: A structural study of the Cantabrian
1218 orocline, NW Iberian Massif. *Lithosphere*, **7**, 653–661, GeoScienceWorld. doi:10.1130/L461.1
- 1219 Sitter, L.U. de & Zwart, H.J. (1957) Geological map of the Paleozoic of the Central Pyrenees. *Leidse Geologische Mededelingen*, **22**, 351–
1220 418.

- 1221 Stampfli, G.M., Hochard, C., Vérard, C., Wilhem, C. & VonRaumer, J. (2013) The Formation of Pangea. *Tectonophysics*, **593**, 1–19.
1222 doi:10.1016/j.tecto.2013.02.037
- 1223 Sussman, A. J., Butler, R. F., Dinarès-Turell, J., & Vergés, J. (2004). Vertical-axis rotation of a foreland fold and implications for orogenic
1224 curvature: an example from the Southern Pyrenees, Spain. *Earth and Planetary Science Letters*, *218*(3-4), 435-449.
- 1225 Tait, J. (1999) New Early Devonian paleomagnetic data from NW France: Paleogeography and implications for the Armorican
1226 microplate hypothesis. *Journal of Geophysical Research*, **104**, PP. 2831–2839. doi:10.1029/98JB02787
- 1227 Tait, J., Bachtadse, V. & Soffel, H. (1994) New palaeomagnetic constraints on the position of central Bohemia during Early Ordovician
1228 times. *Geophysical Journal International*, **116**, 131–140. doi:10.1111/j.1365-246X.1994.tb02132.x
- 1229 Tait, J. A., Bachtadse, V., & Dinarès-Turell, J. (2000). Paleomagnetism of Siluro-Devonian sequences, NE Spain. *Journal of Geophysical*
1230 *Research: Solid Earth*, *105*(B10), 23595-23603.
- 1231 Teixell, A. (1996). The Ansó transect of the southern Pyrenees: basement and cover thrust geometries. *Journal of the Geological Society*,
1232 *153*(2), 301-310.
- 1233 Teixell, A., & Muñoz, J. A. (2000). Evolución tectono-sedimentaria del Pirineo meridional durante el Terciario: una síntesis basada en
1234 la transversal del río Noguera Ribagorçana. *Revista de la Sociedad Geológica de España*, *13*, 251-264.
- 1235 Torsvik, T.H., Voo, R.V.D., Preeden, U., Mac, C., Steinberger, B., Doubrovine, P.V., Hinsbergen, D.J.J.V., *et al.* (2012) Phanerozoic
1236 polar wander, palaeogeography and dynamics. *Earth-Science Reviews*, **114**, 325–368, Elsevier B.V.
1237 doi:10.1016/j.earscirev.2012.06.007
- 1238 Van Dongen, P. G. (1967). The rotation of Spain: palaeomagnetic evidence from the eastern Pyrenees. *Palaeogeography,*
1239 *Palaeoclimatology, Palaeoecology*, *3*, 417-432.
- 1240 van der Lingen, G. J. (1960). Geology of the Spanish Pyrenees, north of Canfranc, Huesca province (Doctoral dissertation, Instituto di
1241 investigaciones geológicas). *Estudios Geológicos XVI*, 206-242
- 1242 Van der Voo, R. (1969). Paleomagnetic evidence for the rotation of the Iberian Peninsula. *Tectonophysics*, *7*(1), 5-56.
- 1243 Van der Voo, R. (1993). *Paleomagnetism of the Atlantic, Tethys and Iapetus oceans*. Cambridge University Press.
- 1244 Van der Voo, R., & Torsvik, T. H. (2012). The history of remagnetization of sedimentary rocks: deceptions, developments and
1245 discoveries. *Geological Society, London, Special Publications*, *371*(1), 23-53.

- 1246 van Velzen, A.J. & Zijdeveld, J.D.A. (1995) Effects of weathering on single-domain magnetite in Early Pliocene marine marls.
1247 *Geophysical Journal International*, **121**, 267–278. doi:10.1111/j.1365-246X.1995.tb03526.x
- 1248 Villalaín, J. J., Casas-Sainz, A. M., & Soto, R. (2016). Reconstruction of inverted sedimentary basins from syn-tectonic remagnetizations.
1249 A methodological proposal. Geological Society, London, Special Publications, 425(1), 233-246.
- 1250 Vine, F.J. & Matthews, D.H. (1963) Magnetic Anomalies Over Oceanic Ridges. *Nature*, **199**, 947–949, Nature Publishing Group.
1251 doi:10.1038/199947a0
- 1252 Vissers, R.L.M. & Meijer, P.Th. (2012) Mesozoic rotation of Iberia: Subduction in the Pyrenees? *Earth-Science Reviews*, **110**, 93–110.
1253 doi:10.1016/j.earscirev.2011.11.001
- 1254 Waldner, M (2019). Cinématique et thermicité du prisme orogénique des Pyrénées : nouvelles données géo-thermochronologiques de
1255 la Zone Axiale. Sciences de la Terre. Sorbonne Université, 2019.
- 1256 Weil, A. B, Gutiérrez-Alonso, G. & Conan, J. (2010) New time constraints on lithospheric-scale oroclinal bending of the Ibero-
1257 Armorican Arc: a palaeomagnetic study of earliest Permian rocks from Iberia. *Journal of the Geological Society*, **167**, 127–143.
1258 doi:10.1144/0016-76492009-002
- 1259 Weil, A. B, Voo, R. van der & Pluijm, B.A. van der. (2001) Oroclinal bending and evidence against the Pangea megashear: The Cantabria-
1260 Asturias arc (northern Spain). *Geology*, **29**, 991–994.
- 1261 Weil, Arlo B, Van der Voo, R. & Voo, R.V.D. (2002) Insights into the mechanism for orogen-related carbonate remagnetization from
1262 growth of authigenic Fe-oxide: A scanning electron microscopy and rock magnetic study of Devonian carbonates from northern
1263 Spain. *Journal of Geophysical Research-Solid Earth*, **107**, 14–14.
- 1264 Weil, Arlo Brandon, Gutiérrez-Alonso, G. & Wicks, D. (2013) Investigating the kinematics of local thrust sheet rotation in the limb of
1265 an orocline: a paleomagnetic and structural analysis of the Esla tectonic unit, Cantabrian–Asturian Arc, NW Iberia. *Int J Earth
1266 Sci (Geol Rundsch)*, **102**, 43–60. doi:10.1007/s00531-012-0790-3
- 1267 Weltje, G.J. (1997) End-member modeling of compositional data: Numerical-statistical algorithms for solving the explicit mixing
1268 problem. *Mathematical Geology*, **29**, 503–549. doi:10.1007/BF02775085
- 1269 Zijdeveld, J. D. A. (1967). AC demagnetization of rocks: analysis of results. In *Methods in Paleomagnetism*, Eds D.W. Collinson, K.M.
1270 Creen and S.K. Runcorn, Elsevier, Amsterdam.

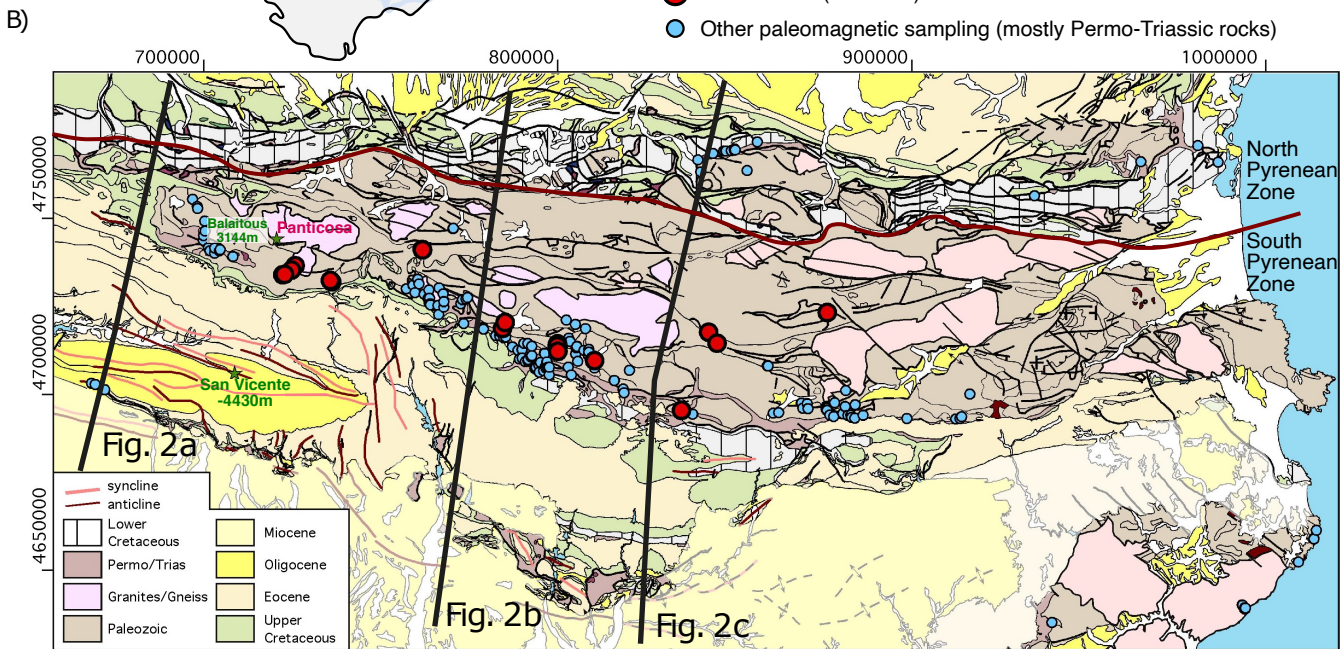
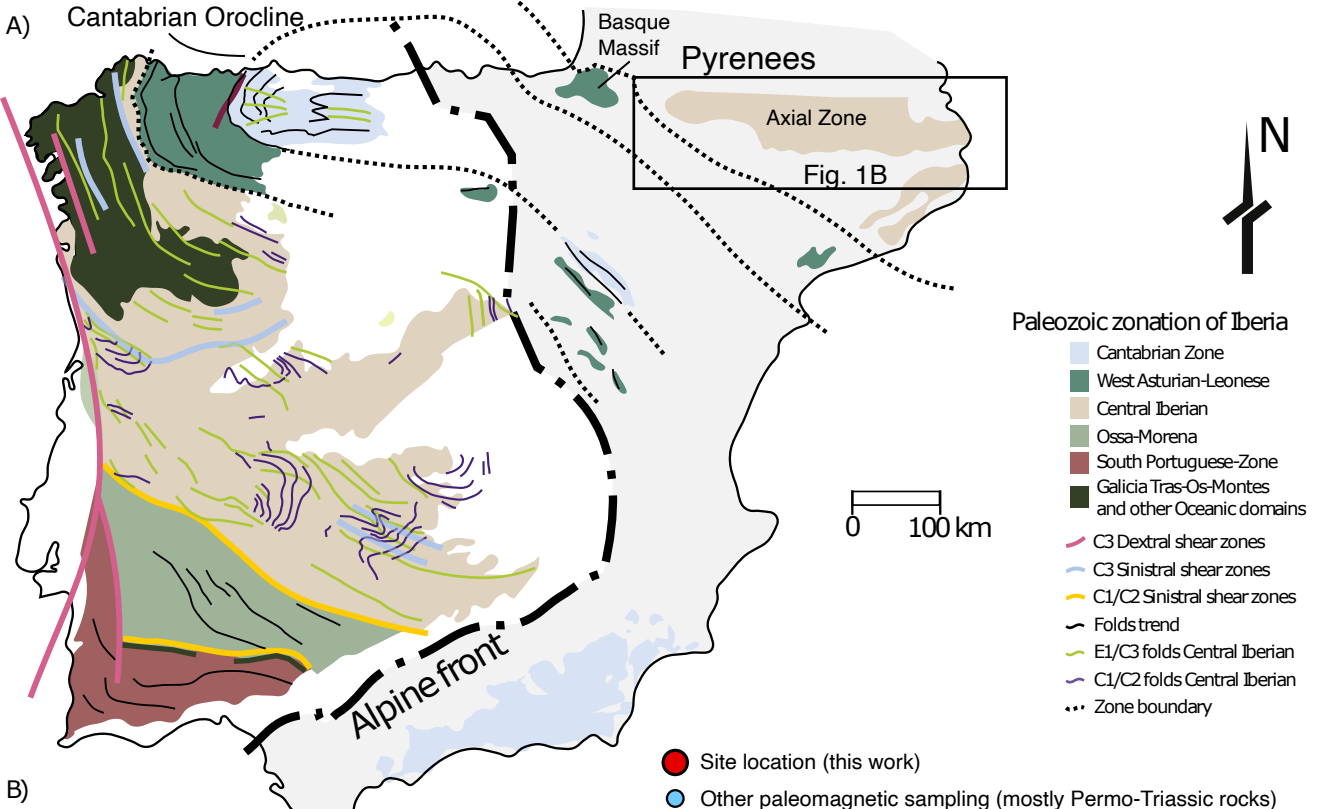


Figure 1: A) Simplified map of the Iberian Peninsula showing the main Paleozoic outcrops and the areas affected by the Alpine orogeny (after Pastor-Galán et al., 2020). B) Geological map of the Pyrenees (modified from Barnolas et al., 2008 according to Choukroune and Seguret, 1973) showing our sampling locations (red dots) and the extensive paleomagnetic studies in the Pyrenees focused mainly

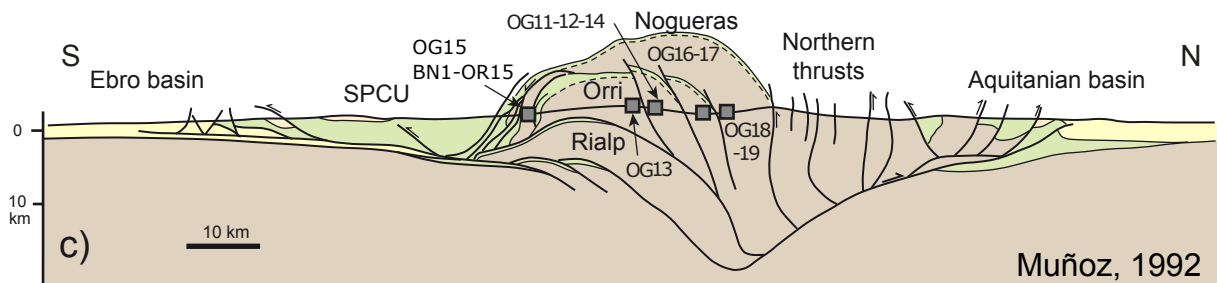
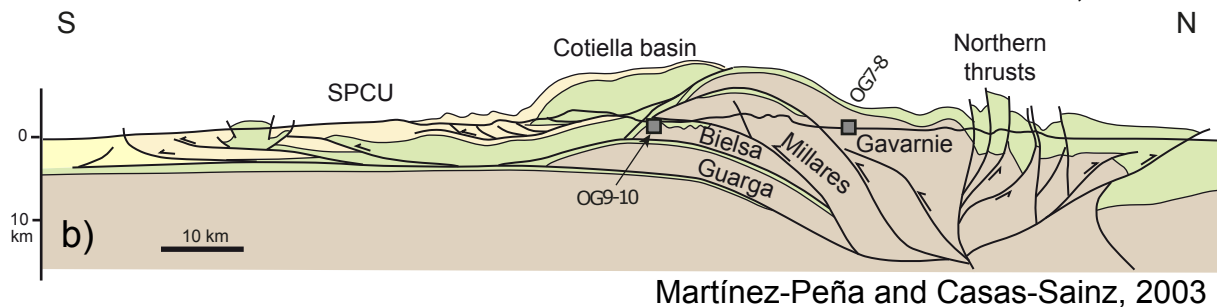
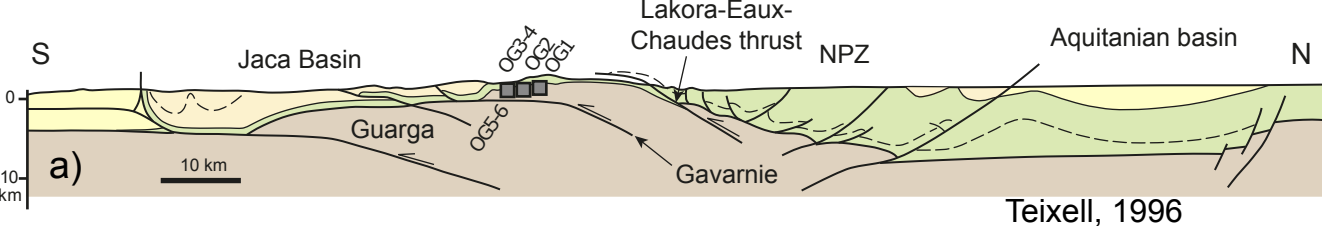


Figure 2: Cross sections through the Pyrenees with projected positions of our sampling sites. The cross-section in a) is from Teixell (1996) whereas cross-sections in b) and c) are from Martínez-Peña and Casas-Sainz (2003) and Muñoz (1992), respectively.

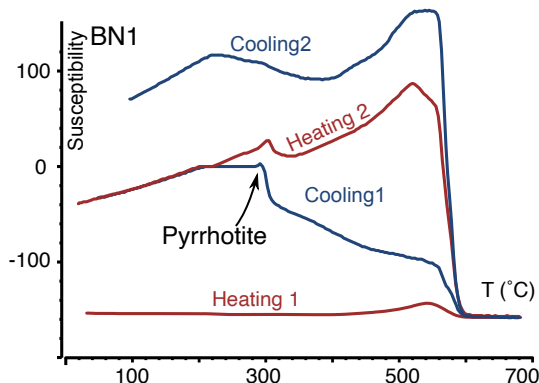
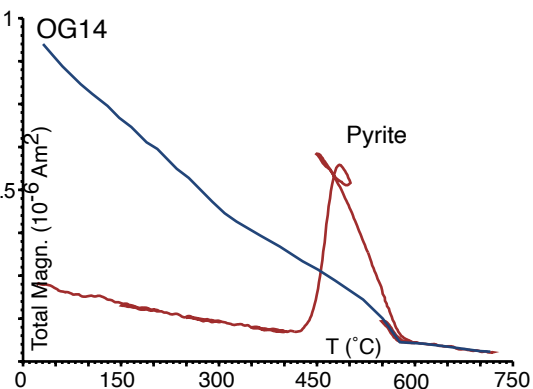
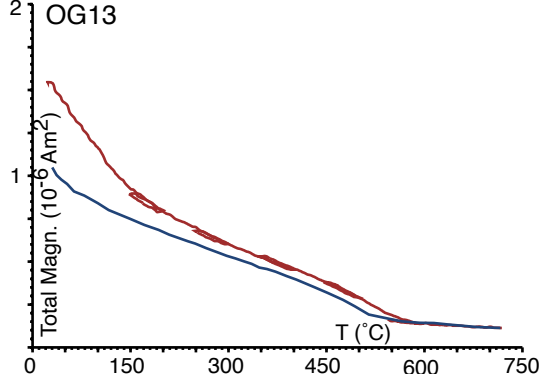
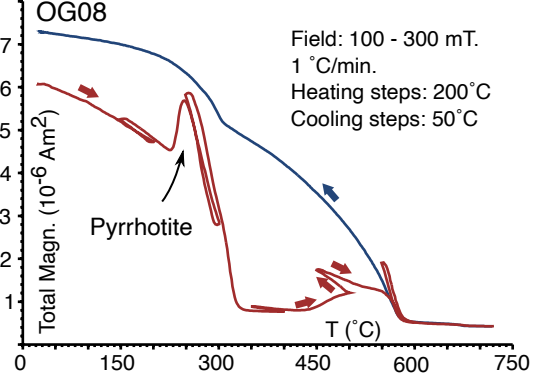


Figure 3: Selected magnetization vs. temperature curves (OG8, OG13, OG14) and susceptibility vs. temperature (BN1). Note that magnetic and non magnetic sulfides are common. All measurements performed are available in supplementary file SF1.

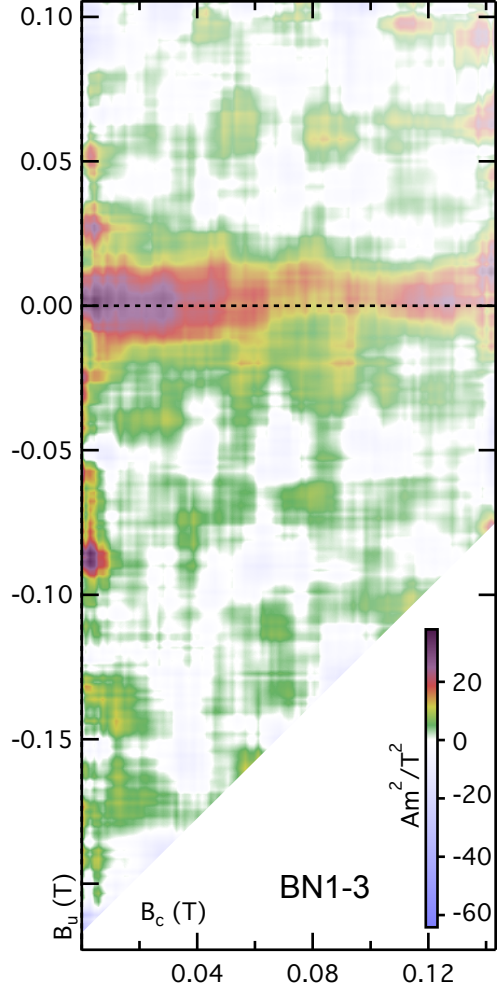
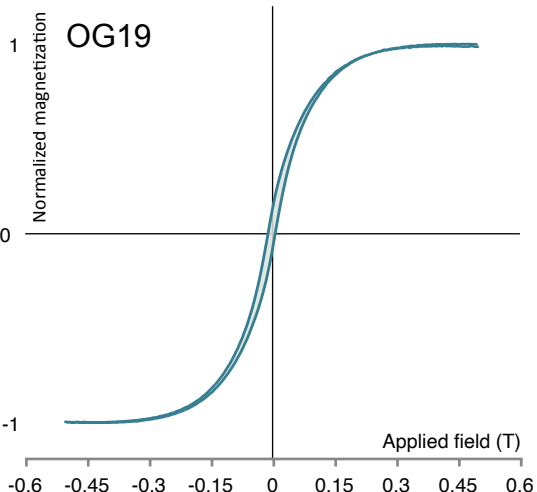
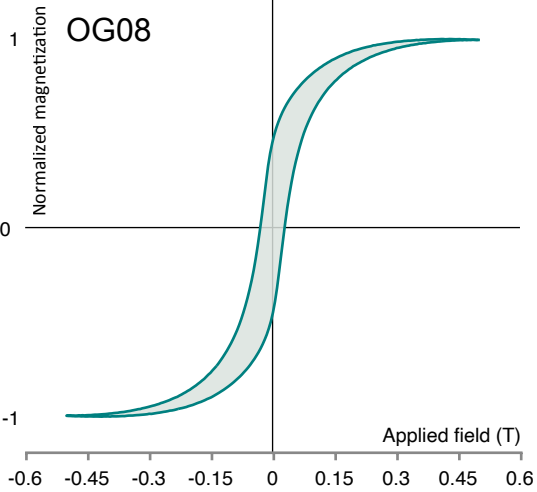


Figure 4: Selected slope corrected hysteresis loops and FORC diagram (plotted with FORCINEL (Harrison and Feinberg, 2008, smoothing factor 13). All measurements performed are available in supplementary file SF2.

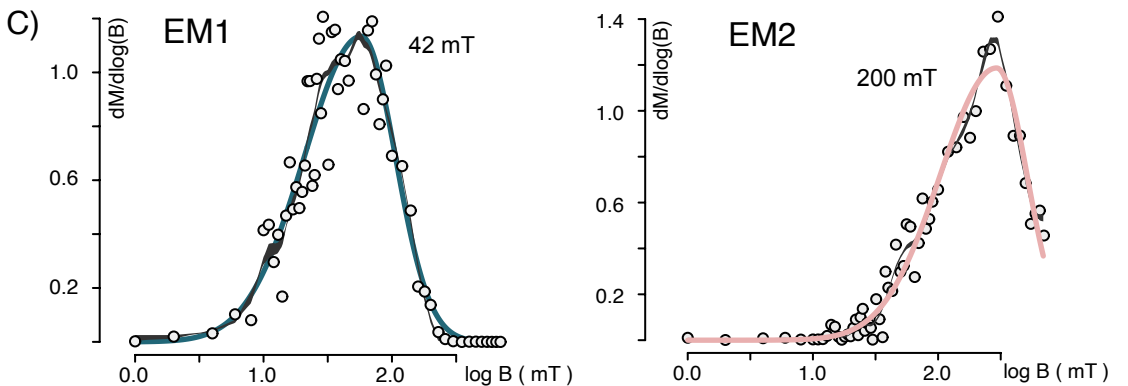
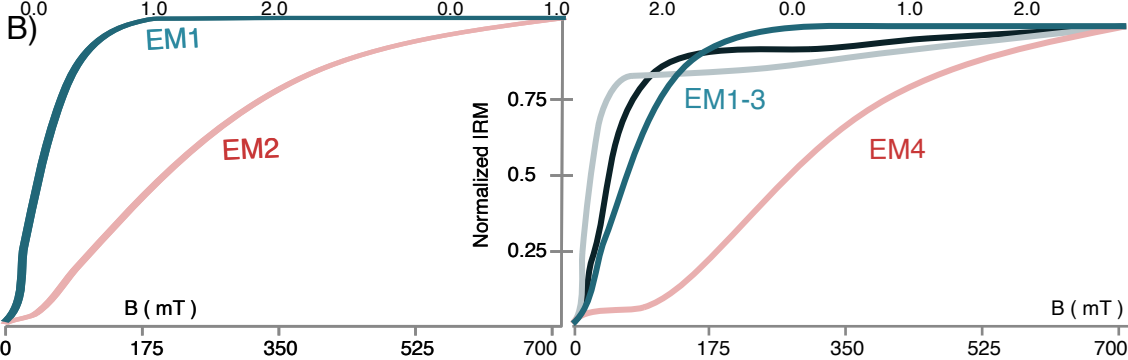
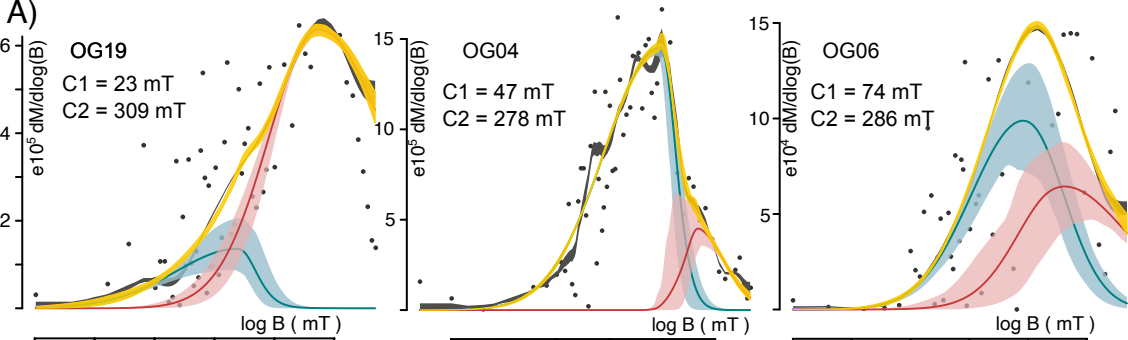


Figure 5: A) Unmixing of IRM acquisition curve for three samples showing different proportions of a 'soft' mineral that saturates below 75 mT (magnetite) and a 'harder' one that saturates over 200 mT (pyrrhotite). B) Results from the endmember modeling showing our preferred two end-member solution (left) and the four end-member solution (right). C) Unmixing of the IRM synthetic acquisition curve from the two end members showing the same two magnetic mineralogies as in the forward modeling of different samples: magnetite to the left and pyrrhotite to the right.

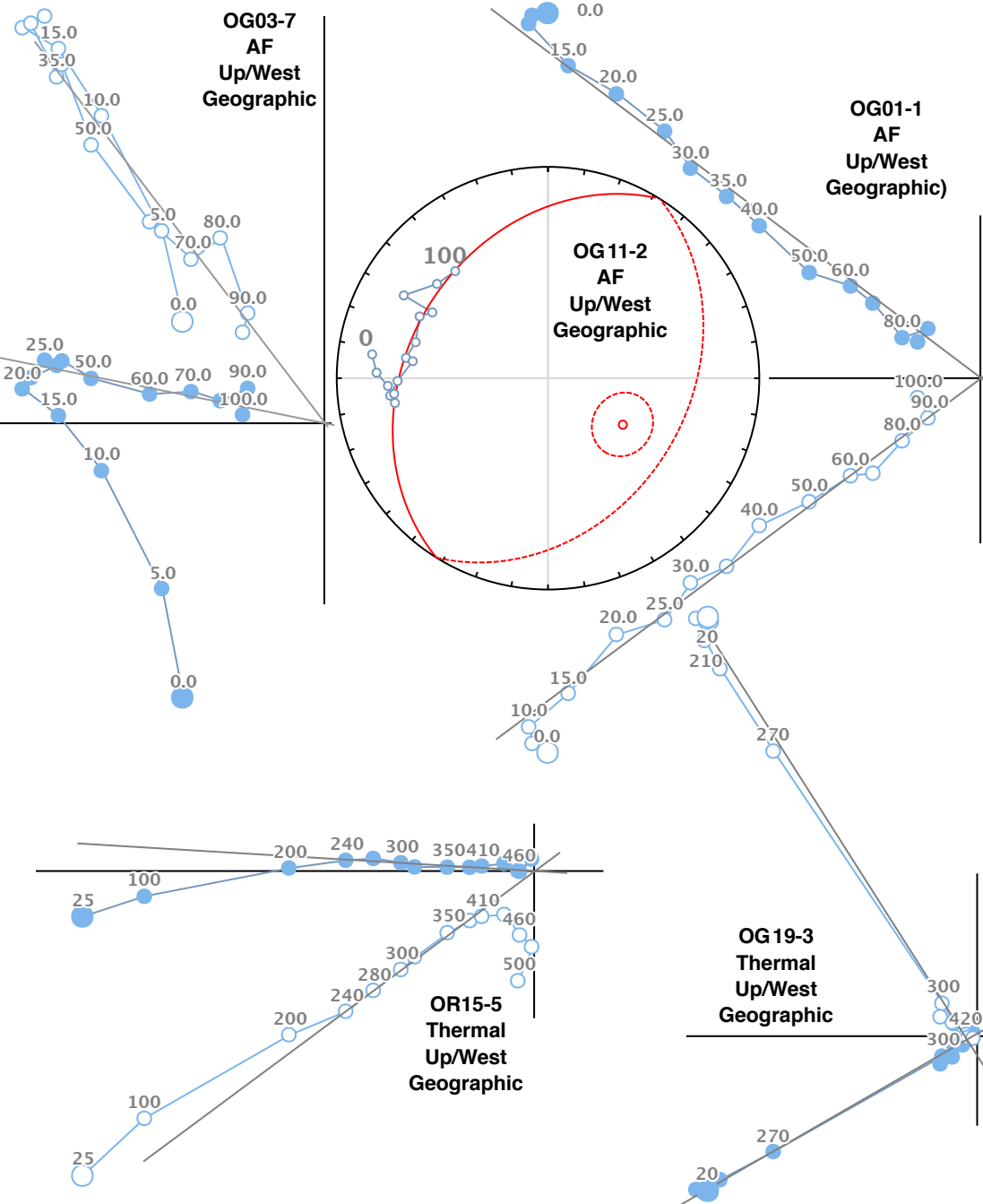


Figure 6: Examples of 'Zijderveld' vector-end point plots (Zijderveld, 1967) for selected samples. All samples plotted in geographic coordinates. Close-open circles represent declination and inclination projections respectively. Complete analyses are available in paleomagnetism.org through the Persistent identifier PID given in the acknowledgements.

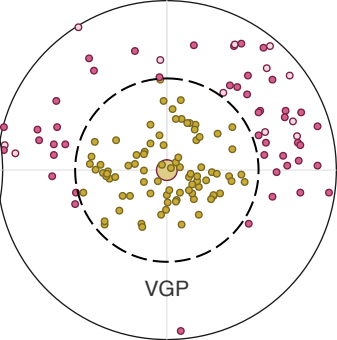
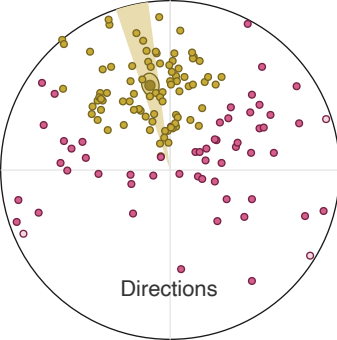
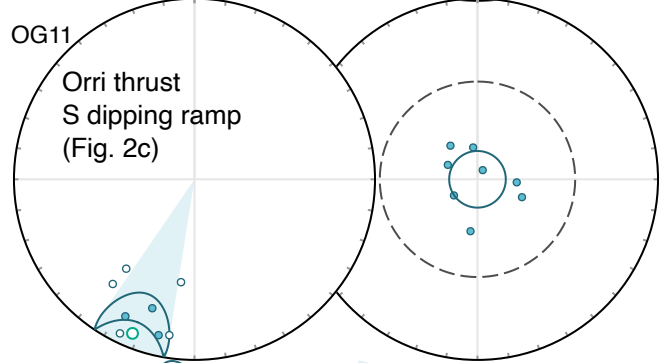
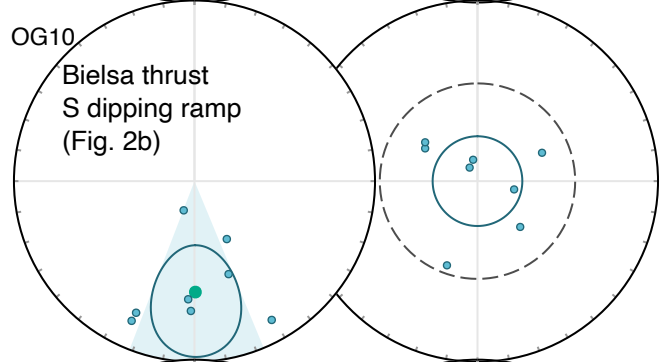
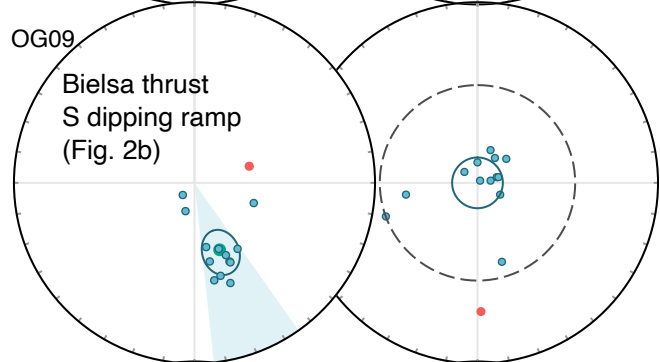
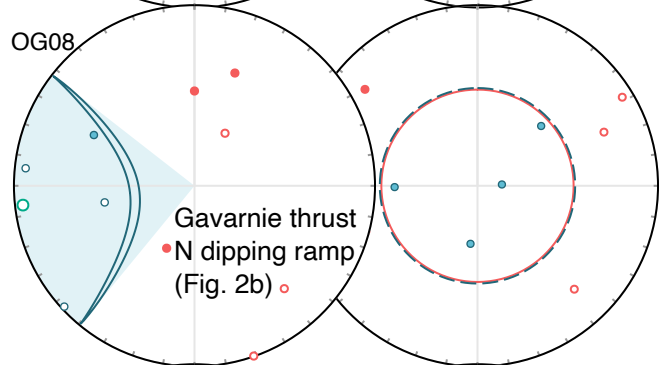
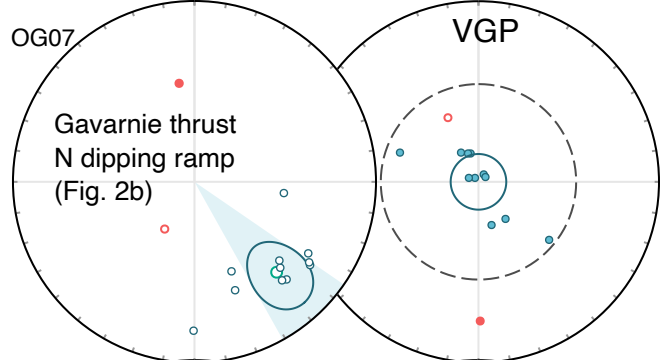
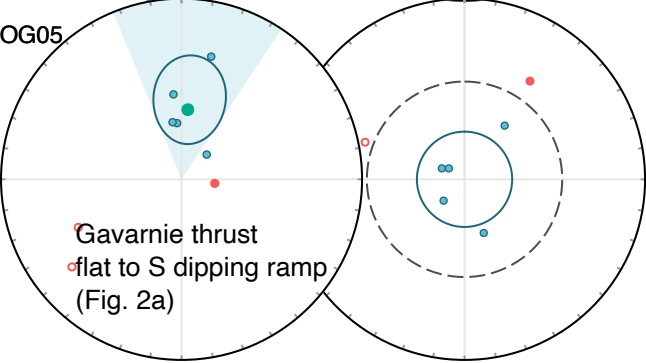
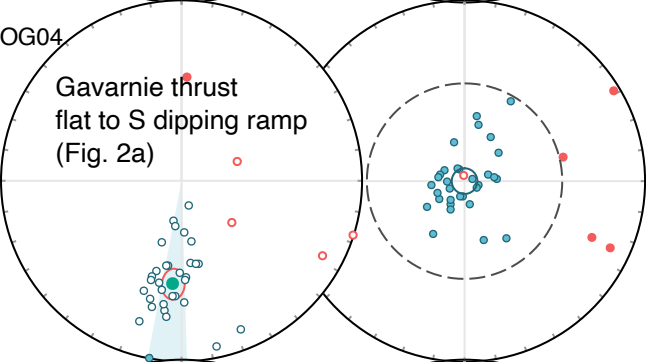
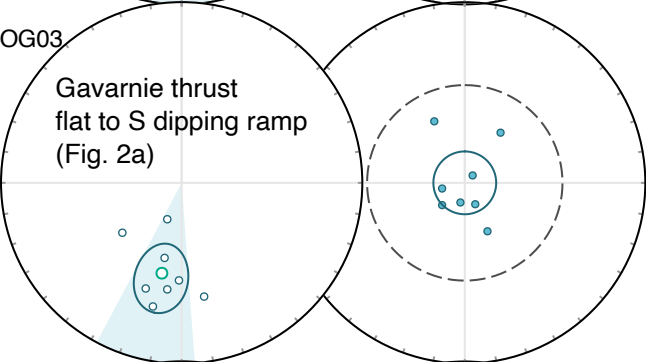
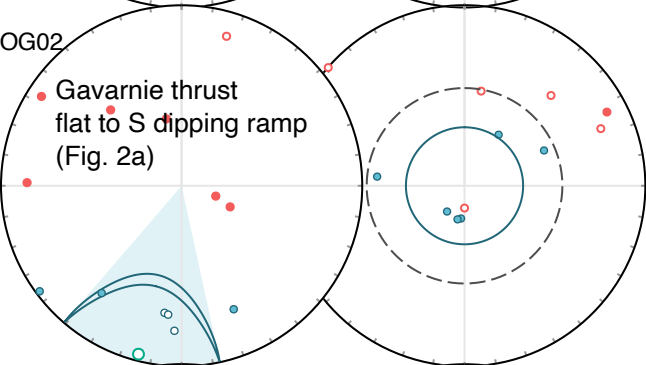
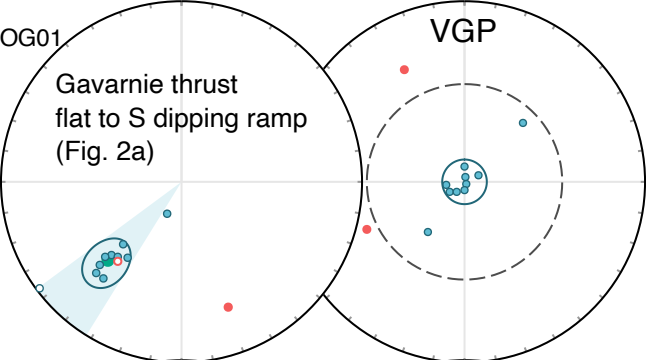
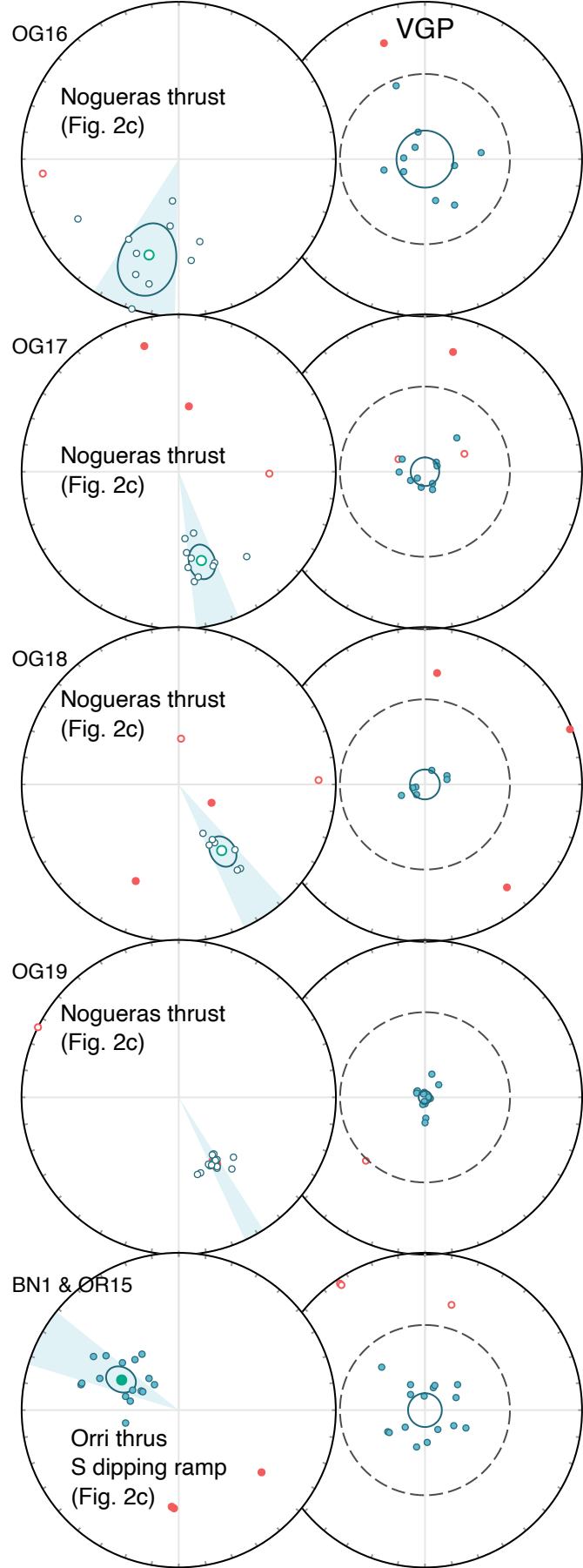
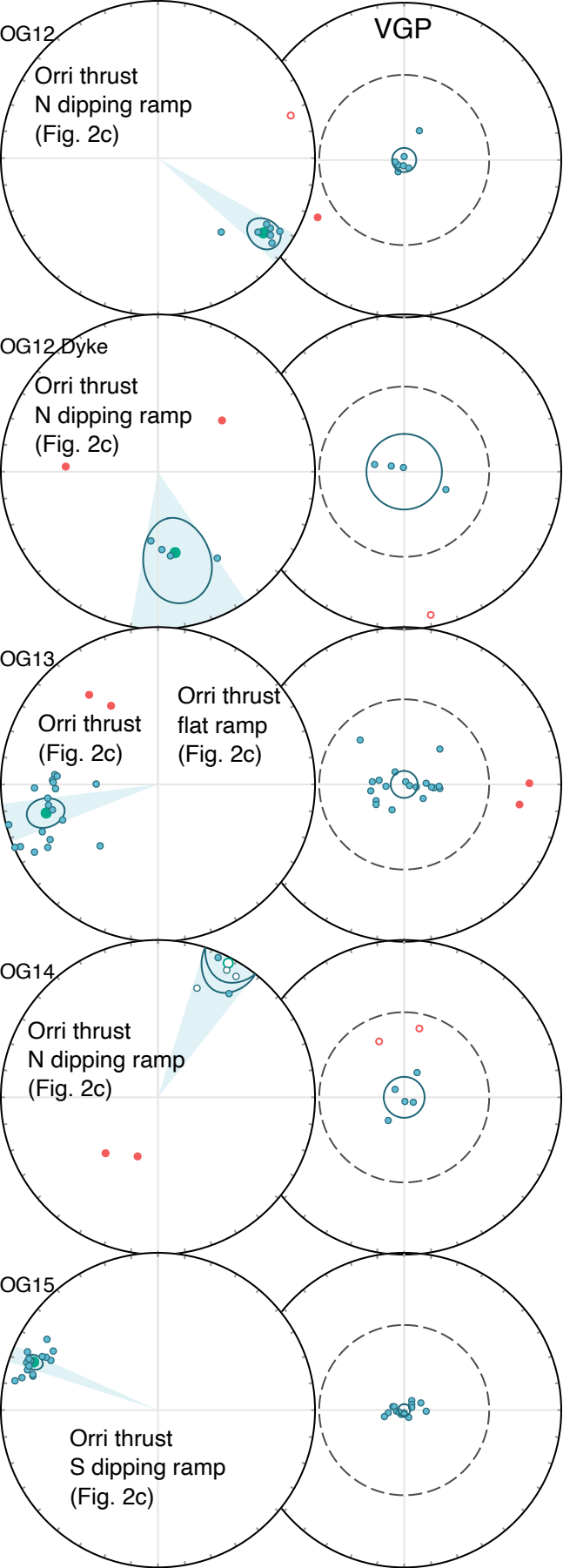


Figure 7: Viscous remanent magnetization (VRM) from all samples is compatible with the present-day field (geographic coordinates). Red dots are those that fall outside of the 45° cut-off. Uncertainty envelope is in both cases VGP A95. The rather large scattering is likely due to the small number of demagnetization levels containing the VRM (3-4) and the possible migration of the VRM during transport, storage and analysis.



● ○ Directions (lower/upper hemisphere)
 ● ○ Rejected directions (lower/upper hemisphere)
 ● Average and A_{95}
▲ ΔD Confidence

Figure 8: Directional and VGP results in geographic coordinates of sites OG01 to OG11. Uncertainty envelope is in both cases VGP A95. Red dots are those that fall outside of the 45° cut-off. Sites OG02, 05 and 08 did not provide statistically meaningful results and were not interpreted.



● Directions (lower/upper hemisphere)
 ● Rejected directions (lower/upper hemisphere)
 Average and A_{95}
 ΔD Confidence

Figure 9: Directional and VGP results in geographic coordinates of sites OG12 to OG19 and BN1-OR15. Uncertainty envelope is in both cases VGP A95. Red dots are those that fall outside of the 45° cut-off. Sites OG02, 05 and 08 did not provide statistically meaningful results and were not interpreted.

(maximum eigenvalue)

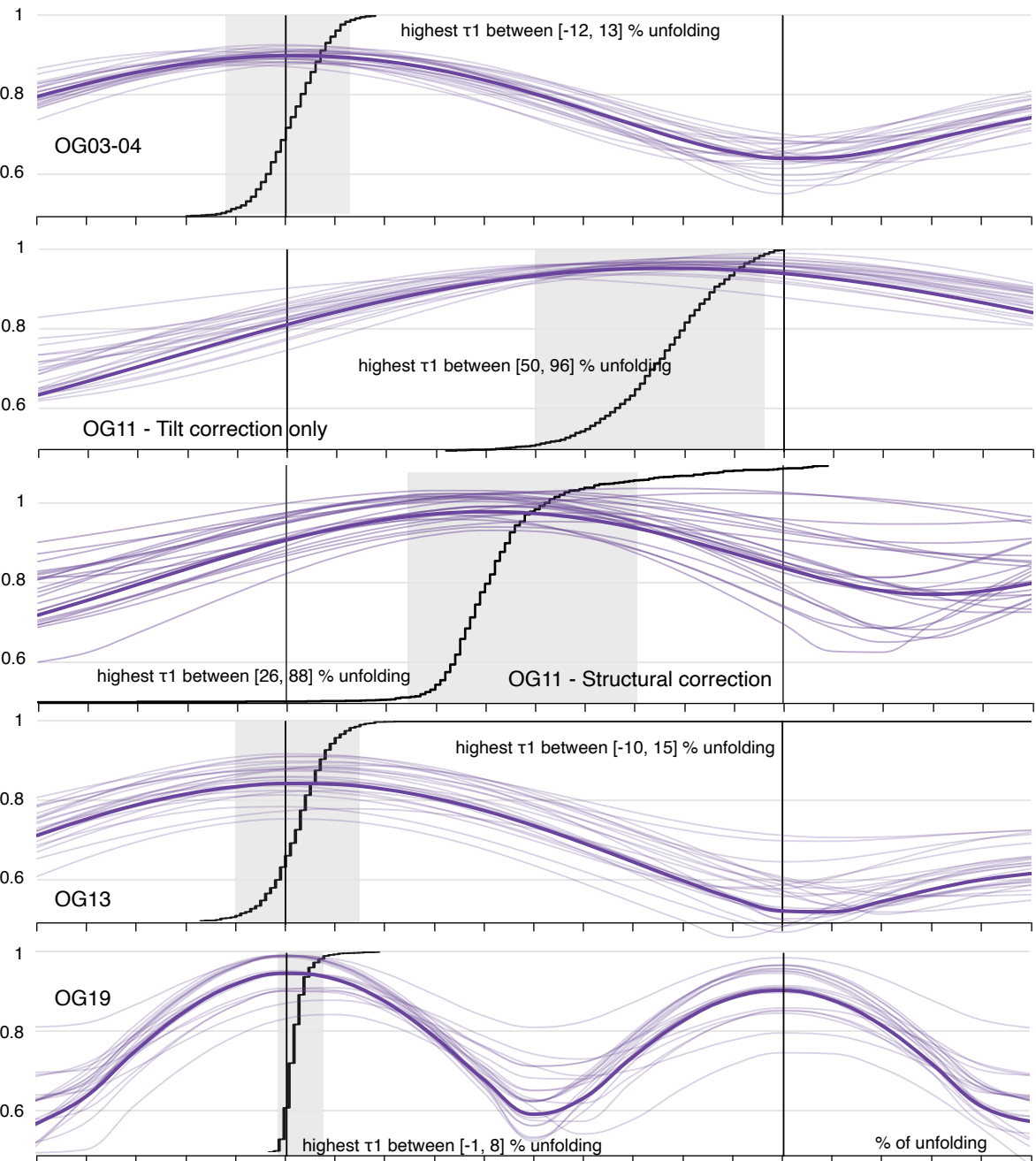


Figure 10: Within-site fold tests. All are negative but OG11, which is inconclusive.

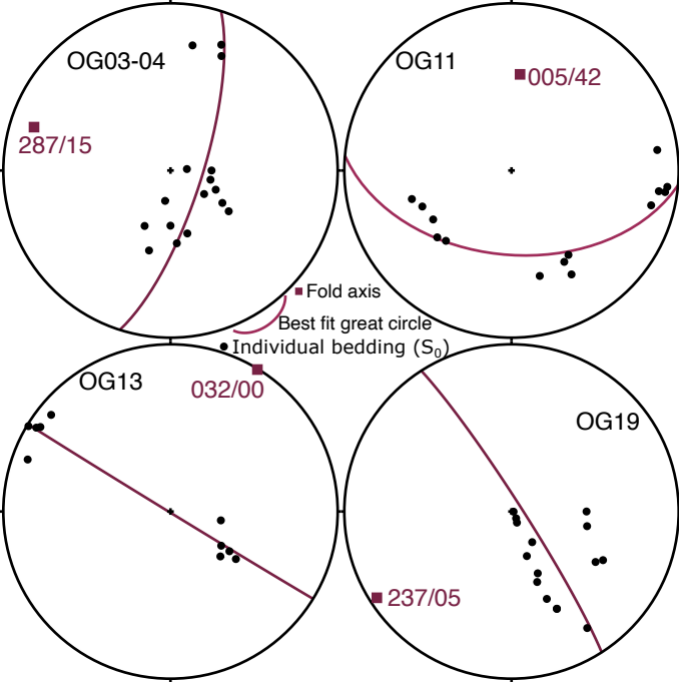


Figure 11: Pi diagrams for the studied folds. Only OG11 shows a steeply plunging axis.

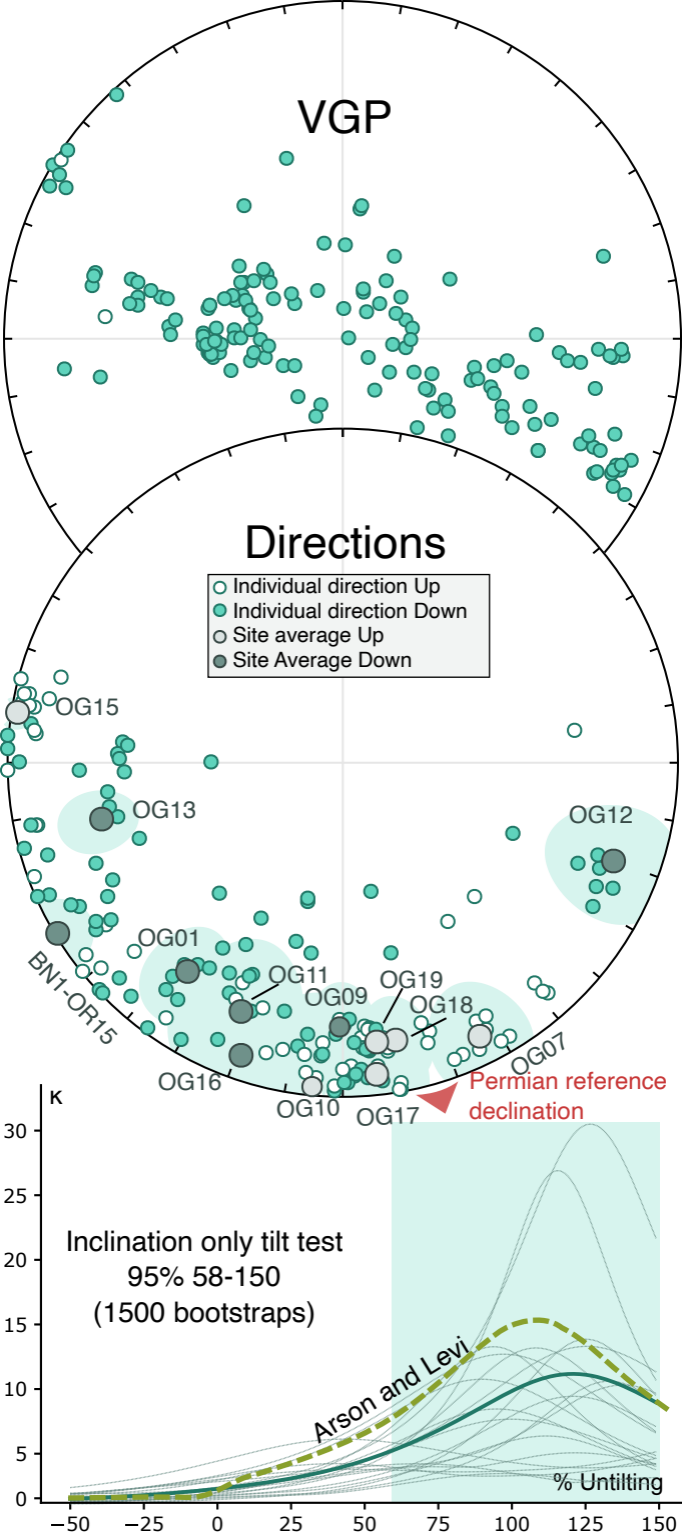


Figure 12: Results after the inferred Alpine tilt correction. Permian reference declination for Iberia is after Weil et al. (2010). The results show a positive inclination only tilt test following the methodology of Enkin and Watson (1996) (selected bootstraps in thin gray lines) and Arson and Levi (2010) approach (dashed line).

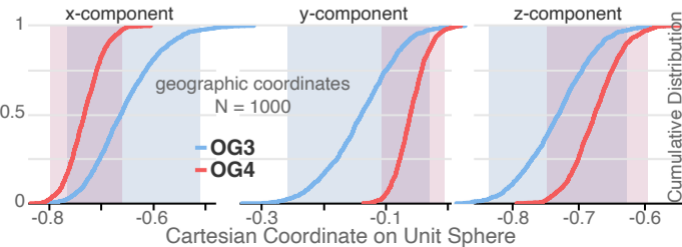
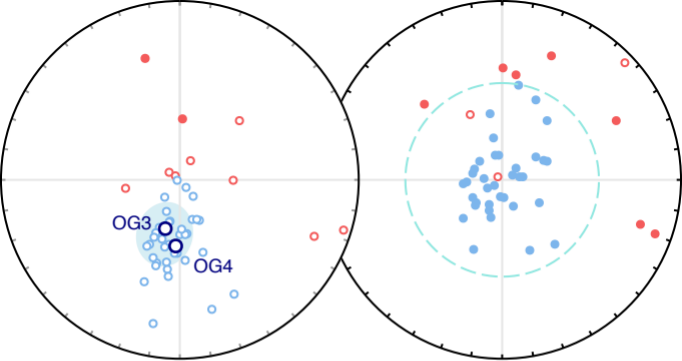


Figure 13: OG03 and OG04 show a common true mean bootstrapped direction (after Tauxe, 2010) in geographic coordinates (and Alpine tilt corrected, since it is the same for both).

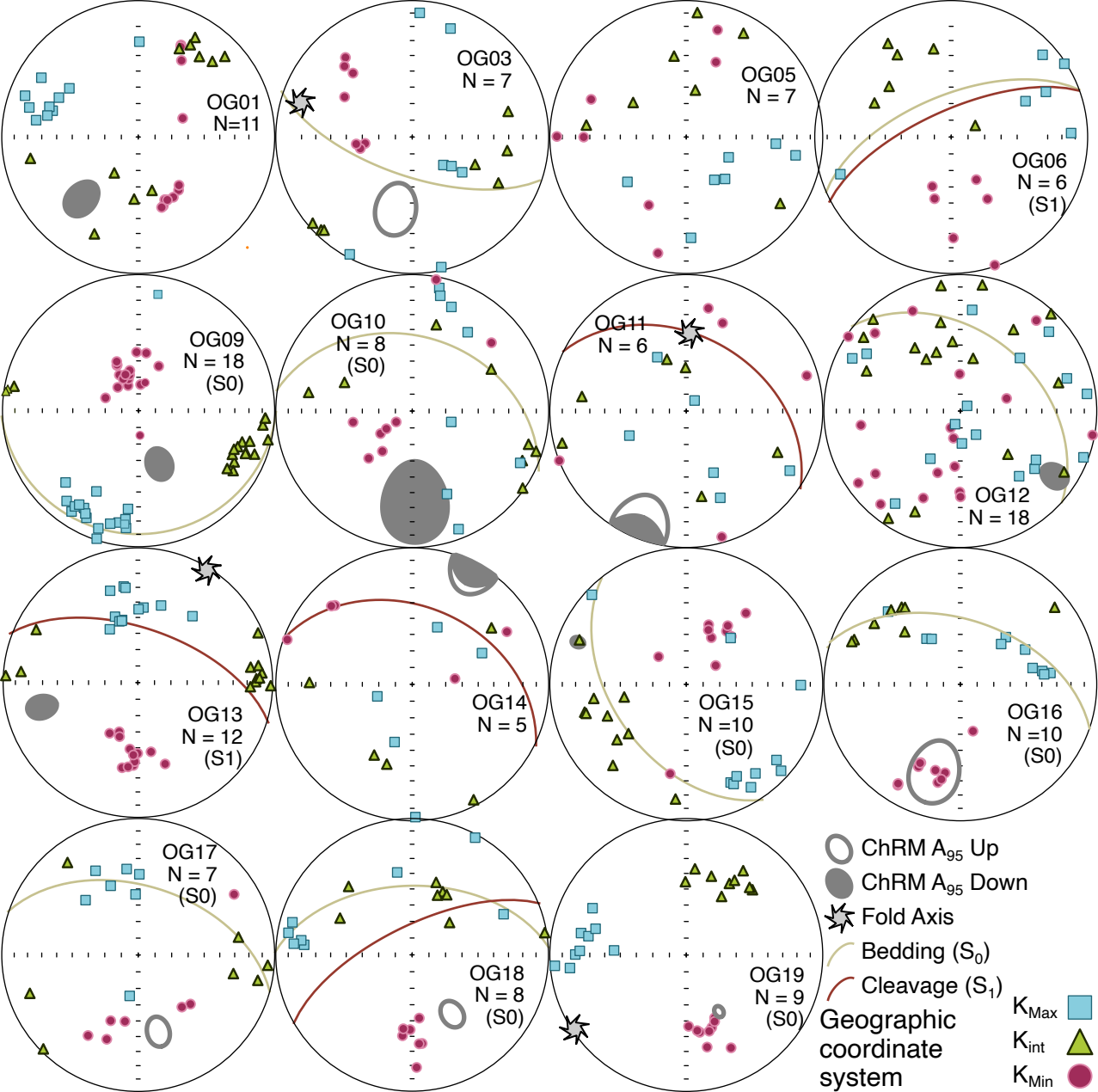


Figure 14: Results from the anisotropy of the magnetic susceptibility analyses. Magnetic fabrics represent bedding or S1 cleavage. Magnetic fabric directions do not coincide with the paleomagnetic directions, which allows us to discard an internal deformation control of the paleomagnetic remanence.

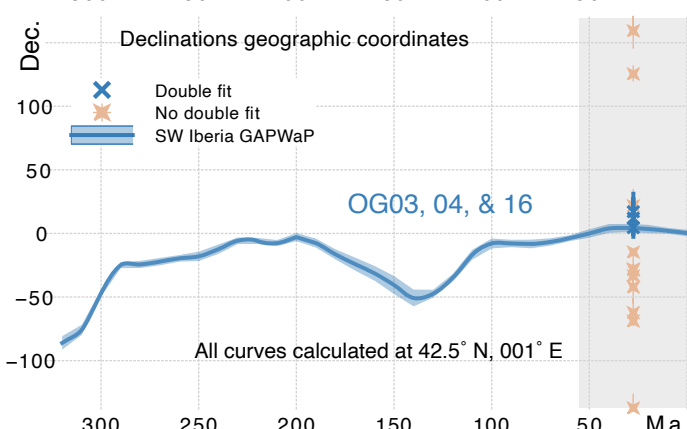
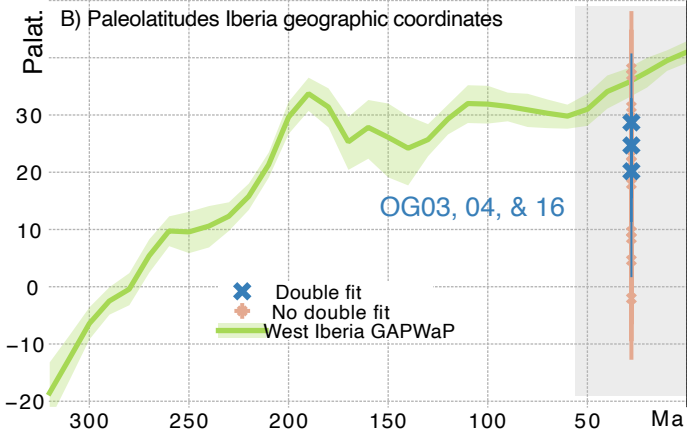
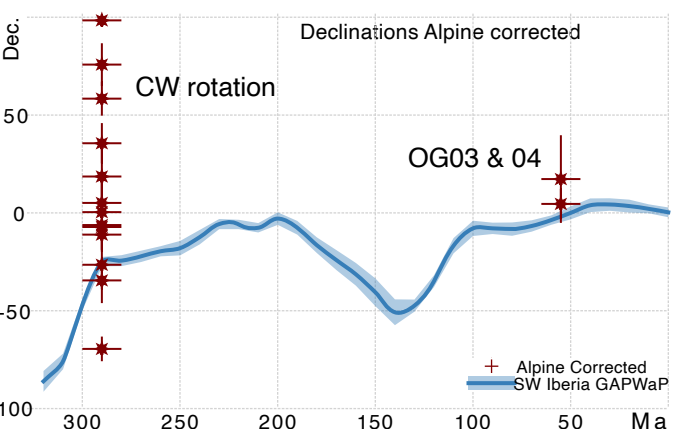
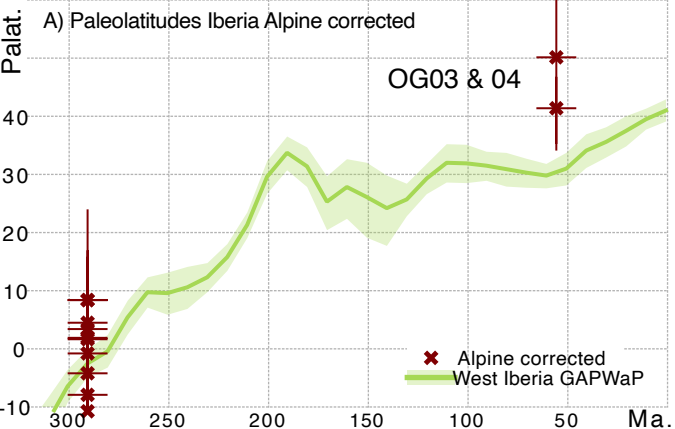


Figure 15: Figure showing paleolatitudes (up) and declinations (down) of OG sites compared to the GAPWaP of Torsvik et al. (2012) rotated to Iberia (following Pastor-Galán et al., 2018). A) After Alpine Tilt B) Geographic coordinates.

Sheet1

Structure	S0 (Bedding)		Fold Axis		S1		Inferred Alpine tilt			Location		
	Dip	Direction	Dip	Trend	Plunge	Dip direction	Dip	Basement thrust unit	Dip Direction	Dip	Latitude	Longitude
OG01	-		-	-	-	-	-	Gavarnie thrust	185	20	42.7473	-0.24497
OG02*		Fold		191	14	-	-	Gavarnie thrust	185	20	42.7361	-0.25841
OG03	199		66	287	15	-	-	Gavarnie thrust	185	20	42.7249	-0.28900
OG04		Fold				20	60	Gavarnie thrust	185	20	42.7259	-0.28300
OG05*	299		17	-	-	-	-	Gavarnie thrust	180	20	42.7023	-0.12022
OG06*	358		62	-	-	256	78	Gavarnie thrust	180	20	42.7064	-0.12464
OG07	36		42	-	-	35	55	Gavarnie thrust	25	45	42.7771	0.19758
OG08*	10		36	-	-	-	-	Gavarnie thrust	25	45	42.7759	0.19858
OG09	89		13	-	-	-	-	Bielsa thrust	205	45	42.5673	0.46444
OG10	17		31	-	-	-	-	Bielsa thrust	205	45	42.5824	0.47447
OG11		Fold		5	42	-	-	Orri thrust	25	30	42.5222	0.65244
OG12	40		39	-	-	-	-	Orri thrust	25	30	42.5167	0.65100
OG13		Fold		32	0	-	-	Orri thrust	25	0	42.5028	0.65228
OG14*		Fold		292	19	-	-	Orri thrust	25	30	42.4752	0.77733
OG15	234		48	-	-	-	-	Nogueras thrust units	205	90	42.3380	1.06883
OG16	16		51	-	-	-	-	Orri thrust	25	45	42.5339	1.17550
OG17	17		50	-	-	-	-	Orri thrust	25	45	42.5048	1.20275
OG18	359		51	-	-	254	67	Gavarnie thrust	25	45	42.5689	1.59106
OG19		Fold		237	5	250	60	Gavarnie thrust	25	45	42.5682	1.58550
BN1 & Of	185		25	-	-	-	-	Nogueras thrust units	205	90	42.3220	1.10466

*Unreliable paleomagnetic result

Table 1

Table 1: Site Location and key structural data from each site.

Sheet1

Geographic	N	Cuto			Dec	Inc	R	k	a95	K	A95	A95min	A95max	ΔDx	ΔIx	λ
		Ns	ff	S												
OG01	10	12	45	16.71	222.7	40.19	9.48	17.3	12	24.19	10	4.78	19.22	10.89	13.79	22.9
OG02*	6	13	45	30.38	194.24	-4.41	4.97	4.86	33.9	7.34	26.5	5.86	26.52	26.52	52.76	-2.21
OG03	8	8	45	20.23	191.98	-47.6	7.66	20.7	12.5	16.32	14.1	5.22	22.12	16.16	16.7	-28.7
OG04	32	37	45	18.08	184.57	-42.53	30.18	17	6.34	20.49	5.75	3	9.24	6.33	7.56	-24.6
OG05*	5	8	45	22.16	5.71	58.01	4.78	17.9	18.6	13.61	21.5	6.3	29.75	28.01	19.81	38.7
OG06*	2	3	45	24.06	248.92	-20.54	1.88	8.48	101	11.42	82.5	9.09	52.99	NaN	149.8	-10.6
OG07	11	13	45	21.77	137.77	-32.97	10.37	15.8	11.8	14.29	12.5	4.6	18.1	13.16	19.46	-18
OG08*	4	10	45	35.85	263.68	-5.38	3.11	3.36	59.5	5.28	44.3	6.89	34.24	44.31	87.91	-2.7
OG09	13	14	45	21.87	159.34	57.48	12.55	26.7	8.18	14.19	11.4	4.3	16.29	14.55	10.64	38.1
OG10	8	8	45	28.26	179.3	38.56	7.17	8.42	20.3	8.45	20.2	5.22	22.12	21.86	28.68	21.7
OG11	8	8	45	18.26	201.72	-9.18	7.18	8.58	20.1	19.89	12.7	5.22	22.12	12.77	24.98	-4.62
OG12	7	8	45	8.33	125.38	18.71	6.89	53	8.36	95.15	6.22	5.51	24.07	6.31	11.48	9.61
OG12-Dyke	4	6	45	16.99	167.95	46.44	3.9	28.8	17.4	23.01	19.6	6.89	34.24	22.23	23.72	27.7
OG13	19	21	45	16.57	255.81	27.7	18.01	18.2	8.09	24.22	6.96	3.7	12.83	7.2	11.67	14.7
OG14*	5	7	45	11.11	27.96	-4.07	4.79	19.1	18	53.41	10.6	6.3	29.75	10.57	21.05	-2.04
OG15	15	15	45	6.56	291.06	16.61	14.87	107	3.71	152.9	3.1	4.06	14.89	3.14	5.82	8.48
OG16	10	11	45	23.96	197.11	-36.31	9.14	10.5	15.7	11.72	14.7	4.78	19.22	15.71	21.7	-20.2
OG17	10	13	45	12.28	165.55	-41.26	9.79	42	7.54	43.86	7.38	4.78	19.22	8.06	9.94	-23.7
OG18	7	11	45	10.29	146.65	-48.47	6.88	49.7	8.64	62.26	7.71	5.51	24.07	8.86	8.94	-29.5
OG19	15	16	45	6.98	151.24	-50.69	14.93	188	2.8	135.3	3.3	4.06	14.89	3.87	3.64	-31.4
BN1 & OR15	16	19	45	18.76	297.88	56.61	15.43	26.1	7.35	18.89	8.71	3.96	14.3	10.96	8.32	37.2
Tilt corrected																
OG01	10	12	45	16.71	222.7	40.19	9.48	17.3	12	24.19	10	4.78	19.22	10.89	13.79	22.9
OG02*	5	13	45	28.84	290.83	0.19	4.02	4.07	43.3	8.09	28.6	6.3	29.75	28.63	57.26	0.1
OG03	8	8	45	24.81	30.57	-65.75	7.66	20.7	12.5	10.9	17.6	5.22	22.12	26.79	13.23	-48
OG04	32	37	45	18.27	179.62	-19.66	29.27	11.4	7.89	19.99	5.83	3	9.24	5.92	10.66	-10.1
OG05*	6	8	45	27.91	19.38	45.79	5.54	10.9	21.2	8.67	24.1	5.86	26.52	27.35	29.65	27.2
OG06*	2	3	45	16.59	230.08	-10.25	1.88	8.48	101	23.93	53.5	9.09	52.99	53.83	104.5	-5.17
OG07	11	13	45	16.8	156.89	-16.86	10.37	15.8	11.8	23.56	9.61	4.6	18.1	9.72	18	-8.62
OG08*	3	10	45	26.69	247.31	-2.42	2.63	5.46	58.9	9.34	42.9	7.73	41.04	42.86	85.58	-1.21
OG09	13	14	45	17.61	164.17	45.05	12.55	26.7	8.18	21.64	9.12	4.3	16.29	10.21	11.39	26.6

Sheet1

OG10	6	8	45	30.89	169.06	56.53	5.52	10.5	21.7	7.09	27	5.86	26.52	34.74	25.85	37.1
OG11	8	8	45	11.72	200.07	-4.48	7.75	27.9	10.7	48.06	8.07	5.22	22.12	8.08	16.07	-2.24
OG12	8	8	45	16.16	111.8	5.44	7.43	12.3	16.5	25.83	11.1	5.22	22.12	11.12	22.06	2.72
OG12-Dyke	4	6	45	19.2	127.4	56.64	3.85	20.5	20.8	18.07	22.2	6.89	34.24	28.35	21.19	37.2
OG13	11	21	45	19.66	183.15	41.74	10.46	18.4	10.9	17.25	11.3	4.6	18.1	12.4	15.1	24
OG14*	5	7	45	21.6	46.47	-55.84	4.79	19.1	18	14.34	20.9	6.3	29.75	26.32	20.34	-36.4
OG15	15	15	45	5.25	289.1	-11.31	14.87	107	3.71	238.1	2.48	4.06	14.89	2.5	4.82	-5.71
OG16	10	11	45	20.18	15.07	-14.68	9.14	10.5	15.7	16.44	12.3	4.78	19.22	12.38	23.37	-7.46
OG17	11	13	45	16.57	171.02	0.43	10.41	16.9	11.5	24.55	9.4	4.6	18.1	9.4	18.8	0.21
OG18	8	11	45	17.99	159.26	-8.83	7.4	11.7	16.9	20.94	12.4	5.22	22.12	12.43	24.35	-4.44
OG19	9	16	45	4.48	155.85	10.2	8.96	217	3.5	327.9	2.85	4.98	20.54	2.86	5.56	5.14
BN1 & OR15	14	19	45	21.46	257.17	56	13.43	22.9	8.49	14.47	10.8	4.18	15.55	13.51	10.49	36.6

* Less than n = 7 was not considered

Table 2

Table 2: Paleomagnetic results for ChRM component for all sites in geographic and tilt (bedding) corrected coordinates.

Sheet1

ALPINE TILT CORRECTION

	Dec	Inc
OG01	215.64	23.55
OG03	197.28	-67.34
OG04	184.57	-60.42
OG07	153.46	-8.93
OG09	145.47	21.97
OG10	180.36	-3.3
OG11	185.14	20.77
OG12	110.54	15.53
OG13	255.81	27.7
OG15	278.36	-3.78
OG16	198.58	8.37
OG17	173.76	-6.78
OG18	168.95	-16.46
OG19	172.82	-16.4
BN1 & OR15	238.36	1.58

Table 3

Table 3: Paleomagnetic results (ChRM) after the Alpine tilt correction (tilt associated to the emplacement of the thrusts).

Sheet1

Inclination only statistics				
Geographic	k	Inclination		α_{95}
Site means avg.		0	0	90
Bedding corrected				
Site means avg.		2.17	18.25	38.91
Site means avg. but OG03 & 04		3.93	22.67	25.44
Alpine tilt corrected				
Site means avg.		4.19	-3.4	21.25
Site means avg. but OG03 & 04		14.42	5.08	11.3

Table 4

Table 4: Concentration parameters of inclination only statistics from the mean values of the sites.